Evidence of a dual African and Australian biomass burning influence on the vertical distribution of aerosol and carbon monoxide over the Southwest Indian Ocean basin in early 2020

Nelson Bègue[1], Alexandre Baron[2,3], Gisèle Krysztofiak[4], Gwenaël Berthet[4], Corinna Kloss*[4], Fabrice Jégou[4], Sergey Khaykin[6], Marion Ranaivombola[1], Tristan Millet[1], Thierry Portafaix, Valentin Duflot[1], Philippe Keckhut[6], Hélène Vérèmes[1], Guillaume Payen[7], Mahesh Kumar Sha[8], Pierre-François Coheur[9], Cathy Clerbaux[9,10], Michaël Sicard[1], Tetsu Sakai[11], Richard Querel[12], Ben Liley[12], Dan Smale[12], Isamu Morino[13], Osamu Uchino[11,13], Tomohiro Nagai[11], Penny Smale[12], John Robinson[12]and Hassan Bencherif[1,5]**

[1] Laboratoire de l'Atmosphère et des Cyclones, UMR 8105 CNRS, Université de la Réunion, Reunion Island, France.

[2] Cooperative Institute for Research in Environmental Sciences (CIRES), University of Colorado, Boulder, CO 80305, USA

[3] NOAA Chemical Sciences Laboratory (CSL), 325 Broadway, Boulder, CO 80305, USA

[4] Laboratoire de Physique et Chimie de l'Environnement et de l'Espace (LPC2E), Université d'Orléans, CNRS UMR7328, Orléans, France.

[5] School of Chemistry and Physics, University of KwaZulu-Natal, Durban 4041, South Africa

[6] Laboratoire Atmosphères, Observations Spatiales (LATMOS), IPSL, UVSQ Université Paris-Saclay, Sorbonne Université, CNRS, Guyancourt, France

[7] Observatoire des Sciences de l'Univers de La Réunion (OSU-Réunion), UAR3365, Saint-Denis de la Réunion, France

[8] Royal Belgian Institute for Space Aeronomy (BIRA-IASB), Brussels, Belgium

[9] Université libre de Bruxelles (ULB), Spectroscopy, Quantum Chemistry and Atmospheric Remote Sensing (SQUARES), Brussels 1050, Belgium; Bruxelles (ULB), Brussels 1050, Belgium.

[10] Laboratoire Atmosphères, Observations Spatiales (LATMOS), IPSL, Sorbonne Université, UVSQ, CNRS, Paris, France

[11] Meteorological Research Institute, 1-1 Nagamine, Tsukuba, Ibaraki 305-0052, Japan

[12] National Institute of Water & Atmospheric Research (NIWA), Lauder, New Zealand

[13] National Institute for Environmental Studies, Tsukuba, Japan

*now at: Institute for Energy and Climate Research - Stratosphere (IEK-7), Forschungszentrum Jülich, Jülich, Germany

**now at: Department for Atmospheric and Climate Research, NILU – Norwegian Institute for Air Research, Kjeller, Norway

Correspondence to: N.Bègue (nelson.begue@univ-reunion.fr)

Abstract

During the 2020 austral summer, the pristine atmosphere of the southwest Indian Ocean (SWIO) basin experienced significant perturbations. This study examines the variability of aerosols and carbon monoxide (CO) over this remote oceanic region and investigates the underlying processes in the upper troposphere – lower stratosphere (UT-LS). Aerosol profiles in January and February 2020 revealed a multi-layer structure in the tropical UT-LS. Numerical models (FLEXPART and MIMOSA) indicated that the lower stratospheric aerosol content was influenced by the intense and persistent stratospheric aerosol layer generated during the 2019-20 extreme Australian bushfire events. A portion of this layer was transported eastward by prevailing easterly winds, leading to increased aerosol extinction profiles over Reunion on January 27th and 28th. Analysis of advected potential vorticity revealed isentropic transport of air masses containing Australian biomass burning aerosols from extra-tropical latitudes to Reunion at the 400 K isentropic level on January 28th. Interestingly, we found that biomass burning (BB) activity in eastern Africa, though weak during this season, significantly influenced (up to 90%) the vertical distribution of CO and aerosols in the upper troposphere over the SWIO basin. Ground-based observations at Reunion confirmed the simultaneous presence of African and Australian aerosol layers. This study provides the first evidence of African BB emissions impacting CO and aerosol distribution in the upper troposphere over the SWIO basin during the convective season.

1. Introduction

Significant amounts of aerosols and trace gases, such as carbon monoxide (CO), are released into the atmosphere during biomass burning (BB) events in the Southern Hemisphere, particularly in Southern America and Southern Africa from July to November (Bencherif et al., 2020; Garstang et al., 1996; Holanda et al., 2020). These activities disrupt the vertical distribution of gases and aerosols, potentially reaching the stratosphere (Andreae and Merlet, 2001; Héron et al., 2020). Under specific meteorological conditions, pyro-convection events can directly inject soot and smoke into the stratosphere (Dowdy and Pepler, 2018; Fromm et al., 2010). The radiative impact of these particles and gases depends on their abundance, vertical distribution, and residence time, influencing their dispersion (Darbyshire et al., 2018; Morgan et al., 2019). Transported over long distances, these aerosols and gases can affect the composition of traditionally aerosol-free regions.

The southwest Indian Ocean (SWIO) basin stands out as one of the Earth's pristine regions where aerosol concentration is predominantly governed by sea salts (Duflot et al., 2022). Characterized by a wet season (December to April) and a dry season (May to November), the SWIO region's atmospheric composition during the dry season is significantly influenced by Southern Hemisphere BB activity (Clain et al., 2009; Edwards et al., 2006; Kaufman et al., 2003; Swap et al., 2003). Studies have highlighted the crossing of BB plumes over South Africa during the dry season, with southern African BB emissions primarily reaching the SWIO basin via five identified transportation modes (Edwards et al., 2006; Garstang et al., 1996). Situated in the subtropical southern Indian Ocean at the convergence of air masses from southern Africa, Reunion Island (21.0°S, 55.5°E) provides an ideal location to study the impact of regional transport on atmospheric composition over the SWIO basin. Ozone radiosonde and ground-based lidar observations at Reunion have revealed a significant annual increase in tropospheric ozone during the August-November period, aligned with the BB season in southern Africa and Madagascar (Clain et al., 2009).

Additionally, long-range transport of BB plumes from South America can influence the tropical tropospheric composition over the SWIO basin (Duflot et al., 2010 2022; Zhou et al., 2018). By combining ground-based observations of carbon monoxide (CO) from a Fourier Transform Infrared (FTIR) spectrometer installed at Reunion with FLEXPART model simulations, Duflot et al. (2010) demonstrated the potential of southern African and southern American BB events to inject substantial amounts of ozone precursors such as CO and aerosols throughout the troposphere over the SWIO basin. This synergy of CO and aerosol observations aids in understanding the influence of BB events on aerosol burden evolution (Bègue et al., 2021; Bencherif et al., 2020; Jones et al., 2001). Recent analysis of Aerosol Optical Depth (AOD) from sun-photometer data at Reunion over 12 years by Duflot et al. (2022) revealed that BB activity explains 67% of AOD variability, with Southern Africa and southern America contributing 22% and 20%, respectively. Despite Australia's reputation for intense BB events (Fromm et al., 2006; 2010; De Laat et al., 2012), its contribution to observed AOD variability over Reunion is relatively low (4.7%).

The Australian BB activity primarily occurs in the northern part of the continent between September and January, although the most severe fires typically occur in southeastern Australia. Extreme fires in this region during the austral summer can lead to pyro-convection events, with a significant impact on the stratosphere at regional and global scales. The unprecedented 2019-

20 fire season, known as the "Black Summer," witnessed numerous pyro-convection outbreaks, injecting approximately 0.9 Tg of smoke into the stratosphere (Yu et al., 2021). This smoke mass, containing 2.5% black carbon, induced a 1 K warming in the stratosphere of the Southern Hemisphere mid-latitude for more than 6 months following its injection. The smoke layer was advected by westerly winds, dispersing across all extra-tropical latitudes in the Southern Hemisphere. The optical characteristics of the stratospheric smoke layer were measured by lidar systems in Chile and Argentina, with the smoke layer extending from 9 to over 30 km in height (Ohneiser et al., 2022). The presence of this smoke layer significantly impacted the record-breaking ozone hole over Antarctica in September-November 2020, as reported by Tencé et al. (2022). Despite the extensive research on the impact of Australian fires on the stratospheric composition and circulation over extra-tropical latitudes, relatively little attention has been paid to their influence over tropical/subtropical latitudes.

This study aims to document the transport of the Australian smoke layer in the southern subtropics over the Indian Ocean during the January-February period, corresponding to the wet season in the SWIO basin. The intensity of convective activity during this season, with the presence of the Inter-Tropical Convergence Zone (ITCZ) over the entire basin, often leads to tropical depressions reaching the stage of tropical cyclones (Lashkari et al., 2017; Barthe et al., 2021; Neuman et al., 1993). The Regional Specialized Meteorological Centre (RSMC) at Reunion reported the development of 6 tropical cyclones and 4 tropical storms in the SWIO basin during the cyclonic season 2019-20.

The study is structured as follows: Section 2 outlines the observations and the model employed to investigate aerosol layer transport. Section 3 reviews the formation and transport of the Australian aerosol layer across the Southern Hemisphere. Section 4 analyzes the impact of the Australian BB plume on aerosol and CO variability over the SWIO basin. Section 5 discusses the influence of convective activity on aerosol smoke layer transport over the SWIO basin. Finally, Section 6 provides a summary and future perspectives of the study.

2. Instrumentation and Model description

2.1 Aerosols data sets

The aerosol datasets used in this study resulted mainly from two ground-based observations sites from the Network for the Detection of Atmospheric Composition Change (NDACC, www.ndacc.org) network as well as a suite of spaceborne sensors products.

2.1.1 Lauder ground-based lidar

Measurements of aerosol optical properties at Lauder (45.0˚S; 169.7˚E) have been performed using lidars since 1992. The lidar system, detailed by Sakai et al. (2016), utilizes a Nd:YAG laser beam at 532 nm with linear polarization. The lidar detects Rayleigh-Mie backscattering at 532 nm with parallel and perpendicular components. Extinction and backscatter coefficients were derived using the methodology outlined by Fernald et al. (1984), incorporating an aerosol extinction-to-backscatter ratio, known as the lidar ratio (LR). LR values for January-May 2020 are 88 sr and 60 sr for altitudes above and below 23 km, respectively, determined through signal attenuation methodology described by Uchino et al. (1983) and Young (1995). Aerosol depolarization was computed from the backscatter ratio and the total linear volume depolarization ratio (Sakai et al., 2003), calculated as the ratio of perpendicular to parallel components of the backscattered signal at 532 nm. To analyze aerosol variability attributed to Australian fires, a background profile was defined using measurements taken during periods without significant atmospheric disturbances, such as volcanic eruptions or pyro-convection outbreaks. In this study, the background extinction profile at Lauder was constructed from measurements made between 1997 and 2004.

2.1.2 Reunion Island ground-based lidars

The Atmospheric Physics Observatory of La Réunion (OPAR) serves as a permanent station for long term atmospheric observations (Baray et al., 2013). Two lidar systems operating the Maïdo Observatory, situated at 2200 m above mean sea level (AMSL), retrieve ozone and aerosol profiles in the UV (355 nm) and visible (532 nm) parts of the light spectrum. These systems, LiO3T (532 nm) and LiO3S (355 nm), are described by Baray et al. (2006). Extending from approximately 15 km to the middle stratosphere (~35 km), these lidars provide high-resolution aerosol optical property measurements (extinction, backscatter ratio) with a vertical resolution of 15 m. By employing two distinct wavelengths, the Reunion lidar profiles facilitate the assessment of the Angström exponent of aerosols between 355 nm and 532 nm, providing insight into the aerosol's extinction behavior and microphysical properties, particularly particle size. A small Angström exponent typically indicates a coarse mode driving the aerosol's optical properties. Further details on the Angström exponent, aerosol size, and their relative error concerning extinction properties are elaborated in Baron et al. (2023) and its supplementary information. The inversion process in this study utilized the Klett method (Klett, 1985), assuming a lidar ratio of 60 sr, typical of aged biomass burning (BB) aerosols (Müller et al., 2007). Nine lidar profiles recorded during the January-March 2020 period were employed, with the background extinction profile at Reunion constructed from measurements taken between

2017 and 2019, excluding the perturbation induced by the Calbuco eruption in April 2015 (Bègue et al., 2017).

2.1.3 CALIOP

Cloud-Aerosol Lidar with Orthogonal Polarization (CALIOP) is a nadir pointing lidar orbiting the Earth onboard the Cloud-Aerosol Lidar and Infrared Pathfinder Satellite Observation (CALIPSO) satellite since 2006. CALIOP operates at two wavelengths (532 and 1064 nm) and measures total attenuated backscatter vertical profiles with altitude-varying vertical (30–300 m) and horizontal (300–5000 m) resolution. In the present study, we used CALIOP product version 3.3 level 1B which includes calibrated attenuated backscatter along with collocated meteorological information provided by the National Aeronautics and Space Administration Global Modeling and Assimilation Office (GMAO). These data undergo postprocessing using a treatment described and validated by Vernier et al. (2009). Scattering Ratio (SR) profiles used for the detection of the smoke plume are calculated following the methodology described by Khaykin et al. (2018). Initially, the collocated GMAO data correct the backscatter profiles of molecular attenuation and ozone absorption. Subsequently, the SR was calculated as the ratio of total and molecular backscatter coefficients, with the latter derived from GMAO air density. SR profiles were recalibrated at 36-39 km, following the methodology given by Vernier et al. (2009). Data with depolarization larger than 30 % were discarded to the treatment in order to avoid aliasing cirrus clouds above the thermal tropopause. CALIOP data were obtained from the ACDISC data archive (ftp://acdisc.gsfc.nasa.gov) hosted by NASA Goddard Space Flight Center.

2.1.4 OMPS-LP

The Ozone Mapper and Profiler Suite Limb profiler (OMPS-LP) has been operational on the Suomi National Polar Partnership (NPP) satellite platform since October 2011. In this study, we utilized aerosol extinction profiles from the NASA OMPS data product version 2.0 (Taha et al., 2021). These profiles were retrieved from the limb scattering solar radiation measurements at wavelengths of 510, 600, 675, 745, 869, and 997 nm, chosen to minimize the impact of gaseous absorption. Aerosol extinction measurements are provided from 10 to 40 km altitude on a 1 km vertical grid, resulting in near-global coverage every 3-4 days. The OMPS data were employed to investigate the global transport of aerosol BB plumes and their influence on the aerosol variability over Reunion. Following the recommendation of Taha et al. (2021), we used aerosol extinction measurements at 745 nm. The background extinction profile was constructed using measurements obtained from 2012 to 2014 and from 2016 to 2018, excluding periods affected by the Calbuco eruption (Bègue et al., 2015). The OMPS data are downloaded from: https://ozoneaq.gsfc.nasa.gov/.

Additionally, we utilized aerosol absorbing index (AAI) data from OMPS to characterize the transport of the aerosol BB plume. The AAI enables the detection of absorbing aerosols by quantifying the spectral difference between specific pairs of UV wavelengths. Positive AAI values indicate the presence of UV-absorbing aerosols such as dust and smoke, while negative values suggest non-absorbing aerosols. Values close to zero typically correspond to the presence of clouds. The AAI data used in this work are available on the NASA Earth Data platform: https://earthdata.nasa.gov/earth-observation-data

2.2 CO and water vapor measurements

2.2.1 FTIR

Ground-based Fourier Transform Infrared (FTIR) spectrometers enable the retrieval of total columns and volume mixing ratio profiles of trace gases like CO with high accuracy and precision (Clerbaux et al., 2008; Vigouroux et al., 2015; Zhou et al., 2019). In the present study, FTIR observations from Lauder and Reunion conducted as part of the framework of the NDACC and Total Carbon Column Observing Network (TCCON) networks respectively, are utilized. The FTIR systems and data retrieval methods are extensively described by de Mazière et al. (2018) and Wunch et al. (2015).

At Lauder, CO measurements have been made since the early 1990s using a Bruker high-resolution spectrometer over a wide spectral range (around 600–4500 cm^{-1}). The CO dataset used in this study aligns with that used by Bègue et al., (2021) and Kloss et al., (2019), providing details on spectral measurements, CO retrieval strategy, and derived CO column abundances..CO total columns and volume mixing ratio profiles for the Lauder site, spanning a 48-layer atmosphere (0.37–100 km asl), were obtained from the NDACC website (http://www.ndacc.org).

At Reunion, FTIR measurements have been routinely conducted since 2011 within the TCCON network using a Bruker high-resolution spectrometer. The GGG2014 code (Wunch et al., 2015) was employed to simultaneously retrieve CO and O2 total columns. The column-averaged dry-air mole fraction of CO was then determined as the ratio between the retrieved CO total columns and the total columns of dry air, leveraging the O2 total columns provided by TCCON. CO abundance data for Reunion were sourced from the TCCON database (https://tccondata.org). For this study, the background evolution of CO is established using measurements obtained between 2015 and 2018 (De Mazière et al., 2017).

2.2.2 IASI

The Infrared Atmospheric Sounding Interferometer (IASI) utilizes a Fourier Transform spectrometer to measure chemical species like CO (Clerbaux et al., 2009; Coheur et al., 2009). Operating aboard the three Metop satellites, IASI retrieves CO total and partial columns occurs in near real-time from the nadir radiances measured by the instrument in the thermal infrared covering wavelengths from 6.62 to 15.5 µm. This enables the generation of global distributions for both day and night measurements, covering the troposphere and lower stratosphere. The Fast-Optimal Retrievals on Layers for IASI (FORLI-CO, Hurtmans et al., 2012) was employed to retrieve total and partial CO columns, while also flagging data contaminated by clouds. For this study, CO columns from IASI instruments on Metop-A (operating since 2006) and Metop-B (operating since 2012) are utilized. The IASI products used in this study can be accessed through the AERIS platform: https://iasi.aeris-data.fr/CO.

2.2.3 MLS

The Microwave Limb Sounder (MLS) on board the Aura satellite has been conducting vertical profile measurements of various trace gases in the UT-LS since 2004 (Waters et al., 2006). For this study, CO and water vapor observations (version 5) from January 2017 to January 2020 were utilized, covering a global domain spanning between 10˚S and 25˚S in latitude and 30˚E and 60˚E in longitude . All MLS version 5 retrieval quality flags (quality, status, convergence, and precision) were meticulously followed for all analyses (Livesey et al., 2022). The recommended pressure levels for science applications with CO and water vapor MLS data range from 0.0215 to 215 hPa (Version 5.0x Level 2 and 3 data quality and description document. (nasa.gov)). The CO and water vapor profiles from MLS were obtained from the Atmospheric Composition Data and Information Services Center (ACDISC) archive (ftp://acdisc.gsfc.nasa.gov) hosted by the NASA Goddard Space Flight Center.

2.3 Numerical Modelling

2.3.1 FLEXPART Model

The Lagrangian transport and diffusion model FLEXPART version 10.4 is utilized in this study to simulate the long-range transport of atmospheric tracers (Pisso et al., 2019; Stohl et al., 2005). This version of FLEXPART incorporates improvements in various aspects, including microphysical and chemical parameterizations (Pisso et al., 2019). Source identification was achieved by releasing particles from a receptor location and simulating backward trajectories (Seibert and Franck, 2004). Model calculations rely on ERA5 reanalysis meteorological observations from ECMWF, extracted at 3-hourly intervals with a horizontal resolution of 0.5° × 0.5° and a vertical resolution of 137 hybrid model levels (Hersbach et al., 2020).

The model simulations involved aerosol (Black Carbon-BC and Organic Carbon-OC) and CO tracers, considering removal mechanisms such as dry and wet deposition for aerosols and OH reactions for CO. The parametrization (default values for the scavenging coefficient and the nucleation efficiency and size) for the BC was found in the paper of Grythe et al. (2017) and the chemical parameterization for CO was in default in FLEXPART data but can be found in the reference kinetics database IUPAC (Atkinson et al., 2006). Each simulation consists of 20,000 particles released over Reunion daily, at altitudes between 15 and 19 km every 0.5 km, and traces them backward in time over one month. Simulations of backward trajectories over long periods (1-2 months) have been explored in previous studies (Aliaga et al., 2021; Eckhardt et al., 2017; Xu et al., 2021). The simulations included turbulence parameterization and convection activation (Forster et al.; 2007).

Model outputs were distributed over a regular vertical grid from ground level to 25 km in altitude. Theses outputs were used to assess the residence time of the BB aerosols and CO, as well as their contributions to the variability of aerosol optical properties and CO over the SWIO basin. Discussions were based on emission sensitivity analysis from backward simulations. The residence time of particles was integrated over the entire atmospheric column and latitude to create averaged maps and longitudinal cross-sections, providing insights into the geographical and vertical dispersion of BB aerosols.

The BB contributions to the vertical distribution of CO and the aerosol optical properties were calculated by combining the potential emission sensitivity (PES) with an emission inventory, as explained in Stohl et al. (2003). PES represents FLEXPART particles injected at the layer/altitude of emissions. Pyro-convection was not considered in the model. BB aerosol and CO mass concentration profiles were obtained by summing all output grid points. For BB emissions, a layer between 0 and 3 km was used for Africa and between 9 and 16 km for Australian fires.

The Global Fire Assimilation System (GFAS) version 1.2 emission (Kaiser et al., 2012) and the Global Air Pollutant Emissions - EDGAR v6.1 emission inventory (http://edgar.jrc.ec.europa.eu) for CO were utilized. These emissions represent total CO emissions from anthropogenic activities, excluding large scale BB. Multiplying the CO emission flux from this inventory by the FLEXPART emission sensitivity for a layer between 0 and 1 km provides the contribution of anthropogenic sources to total CO abundance. Finally, aerosol mass concentration profiles are converted into extinction profiles using the Mie scattering model, considering spherical particles with a density of 2 $g.cm^{-3}$ and a refractive index of 2.0 + 0.64i for optically absorbing aerosols.

2.3.2 MIMOSA Model

The Modèle Isentropique de transport Mésoéchelle de l'Ozone Stratosphérique par Advection (MIMOSA) model is a potential vorticity (PV) advection model designed to run on isentropic surfaces with a resolution of $0.3^\circ \times 0.3^\circ$ (Hauchecorne et al., 2002). Its advection scheme is semi-Lagrangian with a time step of 1 h and is driven by ERA5 reanalysis meteorological observations. The model can be continuously run to track the evolution of PV filaments over several months. The accuracy of the MIMOSA model has been evaluated and validated in previous studies. Hauchecorne et al. (2002) assessed its accuracy, and it was validated against airborne lidar ozone measurements using a correlation between PV and ozone, as ozone behaves as a quasi-conserved chemical tracer on timescales of a week or so within most of the lower stratosphere (Heese et al., 2001). Moreover, the MIMOSA model can be used to determine the origin of air masses influencing a given site, similar to an isentropic Lagrangian trajectory model. This capability has been demonstrated in various studies (Bencherif et al., 2011; Hauchecorne et al., 2002; Portafaix et al., 2003; Bègue et al., 2017).

3. Formation of an intense stratospheric BB plume over Australia

Figure 1 shows the AAI obtained from OMPS on bord CALIOP over New-Zealand on 1st January. Following the strongest outbreak during New Year's Eve, a wide plume of BB aerosol with large values of AAI (higher than 12) is transported toward the Tasman Sea on 1st January 2020 (Fig. 1a). The CALIOP attenuated SR profiles are calculated along the CALIOP track (blue line in Fig. 1a) crossing the absorbing aerosol plume above New-Zealand. CALIOP observations reveal a broad region of high values (ranging from 10 to 25) between 36° S and 46°S centered at 16.5 km altitude (Fig. 1b).

Figure 2a illustrates the daily extinction profiles at 532 nm derived from lidar measurements over Lauder (New-Zealand) between 1st December 2019 and 1st April 2020. Note that a strong convective activity prevented lidar operations between mid-December 2019 and the 1st January 2020. Figure 2a reveals high values in the extinction (from 3×10^{-3} km^{-1} to 9×10^{-3} km^{-1}) in the stratosphere over Lauder starting in mid-January 2020, one order of magnitude above the typical stratospheric aerosol background (Sakai et al., 2016). The vertical extent of the plume increased significantly between mid-January and 1st April 2020 with an aerosol layer spanning from 11.5 to 20 km. The ascent of BB aerosol could be due to adiabatic heating effect (De Laat et al., 2012). A statistically significant increase of sAOD (between 15 and 30 km) is observed in January 2020 (2.5 times higher than background value) and still visible in April 2020 with same amplitude (Fig. 2b).

The same observation can be made for the carbon monoxide in the UTLS over New-Zealand, as shown in Figure 3 with the observations made by the FTIR at Lauder. Prior to the convective period, the maximum of CO mixing ratio (120-130 ppbv) is observed in the troposphere (Fig. 3a). An increase of CO mixing ratio in the lower stratosphere is visible from mid-December 2019 with the maximum (50-90 ppbv) observed in the UT-LS (9-13 km). The partial column of CO (between 9 and 30 km), calculated from FTIR, reaches its maximum values (~33 % higher than background value) in January 2020 and slightly decreases in April 2020 (~24% higher than background value) (Fig. 3b). Above the lower stratosphere, the CO mixing ratio decreases significantly due to photochemical reactions which are more efficient with altitude (Brasseur and Solomon, 2005).

Our works suggest that the injection of CO and absorbent aerosols ends up de-correlated in altitude given their different properties. In order to extend the discussion, the spatial dispersion of the Australian BB plume in the Southern Hemisphere will be discussed in the next section.

4. Transport of the Australian BB plume over the SWIO basin

4.1 Aerosol and CO variability over a subtropical site: Reunion

Figure 4 shows time-averaged maps for AOD from OMPS and CO partial column (9-30 km) from IASI observation. The transport of the aerosol (with values ranging from 6×10^{-3} to 1×10^{-2} km^{-1}) and CO (with values ranging from 6 to 8×10^{17} molecules. cm^{-2}) plume over the Southern Pacific occurred mainly within the 18˚S–60˚S latitudinal band. One can observe an aerosol band (with values ranging from 5×10^{-3} to 9×10^{-3} km^{-1}) across the Southern Hemisphere between 40˚S and 60˚S during the 9-16th January 2020 period (Figure 4a). The Australian aerosol plume has already circled the Southern Hemisphere during the first two weeks of January 2020. The same conclusion cannot be made for CO from space-borne observations (Figure 4b). One can observe weak values of CO (less than 5×10^{17} molecule.cm^{-2}) over southern Atlantic and without a real link with the large plume observed over southern Pacific (Fig. 4b).

Figure 5a depicts the evolution of the sAOD at 532 nm calculated between 15 and 30 km from the ground-based lidars and OMPS observations over Reunion from 1st January to 1st March 2020. OMPS extinctions are converted to 532 nm using an Angström exponent for the 532–745 nm wavelength pair of 1.9, as prescribed by Taha et al. (2021). Reunion witnessed an abrupt increase in the aerosol loading (three times above the typical background) as of 16th January 2020 according to satellite observations. The sAOD values observed between 16th January and 1st March 2020 are higher than those observed during the passage of the Calbuco plume over

Reunion site, which did not exceed 0.013 (Bègue et al., 2017). The increase of sAOD in mid-January coincided with an increase of CO, as shown in Figure 5b based on the use of partial columns (between 9 and 30 km) and CO abundance from IASI and FTIR at the same site and over the same period. The ground-based observations show that the CO abundance observed during this increased phase is on average 20% higher than the values observed during the background period (Fig. 5b). The evolution of sAOD and CO observations in mid-January suggests that Reunion, and its surrounding, have been influenced by the transport of the Australian BB plume.

Figure 6 shows aerosol extinction profiles at 355 nm over Reunion for selected days in January or February compared to the January or February background profiles. The two first weeks of January 2020 are representative of the January typical background (shaded area), as illustrated on 13th January 2020 (Fig. 6a). Conversely, the extinction profiles at the end of January 2020 (27th and 28th) are marked by a significant increase (4 times higher than the background values) located in the lower stratosphere between 16.8 and 18 km altitude (equivalent to potential temperature levels 380-404 K). On 28th January, the extinction profile exhibits a sudden increase at 17.4 km (~400 K) and quickly decreased afterwards to values observed the previous day (Fig. 6a). The values of extinction (10 to 17 $\times$ 10^{-3} km^{-1}) observed in the lower stratosphere on these two days are of the same order as those observed at Lauder a few days after the pyro-convective event (Fig. 2). In February, the extinction profiles clearly exhibit two significant aerosol layers with the first one located between 16 and 19.5 km (370-440 K) and the second one between 20 and 22.5 km (465-500 K) (Fig. 6b).

To further discuss the optical properties of these aerosol layers, the Angström exponent has been calculated between 355 nm and 532 nm from the ground-based lidar measurements (Figs. 6c and 6d). In February, the Angström exponent values reveal that the two aerosol layers consist mainly of small aerosol particles (Fig. 6d), consistent with a stratospheric smoke layer (Haarig et al., 2018; Hu et al., 2019; Ohneiser et al., 2021). In January, the profile of Angström exponent exhibits more variability in the UT-LS (Fig. 6c) with values ranging from 0.6 to 1.9, on 27th and 28th January. The wide range of Angström exponent values suggests that the aerosol layer is not homogeneously distributed at this stage and might be interpreted as a mixture of fresh and aged smoke layers (Fig. 6c). Indeed, Müller et al, 2007 showed that ageing of transported smoke translates into a decreasing of the Angström exponent. This may indicate growth and removal processes (e.g., coagulation, condensation, sedimentation) which can modulate the morphology and mixing state of the aerosol layer during its transport (Burton et al., 2015; Hamil et al., 1997).

4.2 Origin of the air masses

To analyze the origin of air masses at Reunion on 27th and 28th January, one-month backward trajectories were calculated using FLEXPART (Aliaga et al., 2021; Eckhardt et al., 2017; Xu et al., 2021). A period of one month was chosen because it refers to the time lapse separating the pyro-convective outbreak event and the day of the measurement at Reunion. The representation of the potential emission sensitivity (PES) from back-trajectories simulations initialized at 18 km originating from Reunion on 27th and 28th January 2020 are presented in Figure 7.

Figures 7A-1 and 7B-1 display the horizontal trajectories, whereas vertical movement is shown in Figures 7A-2 and 7B-2, respectively. The vertical transect of FLEXPART back trajectories in Figure 7A-2 confirms a high probability of air mass contribution from Australia if the fires emissions are directly injected into the stratosphere by convection (black rectangle in the figure), (i.e. layer of 9 to 16 km of injection taken for the PES, see section 2.3.1). According to FLEXPART results, part of the Australian smoke layer is advected zonally by the prevailing easterly winds and is observed over Reunion on 27th and 28th January 2020 at 18 km. The FLEXPART simulations also suggest that Reunion is influenced by eastward transport of air masses. This pathway is clearly visible on 28th January 2020 (Figs. 7B-1 and 7B-2). Air masses from high latitudes seem to cross the subtropical latitudes following a wave shape and reach the SWIO basin by passing over the Cape of Good Hope (Figure 7B-1).

In order to delve further on this eastward transport of air masses over the SWIO basin, the MIMOSA model has been used to produce a continuous evolution of PV fields for the period from 1st to 31st January 2020 for the 400 K isentropic level. The localization of the aerosol plume obtained from OMPS observations at the 400 K ± 5 K isentropic level are also superimposed (Fig. 8). The 400 K isentropic level is chosen according to the layers observed in the extinction profiles over Reunion between 390 and 404 K isentropic level on 27th and 28th January 2020 (Fig. 6a). Air masses from mid-latitudes (40-60˚S) cross the subtropical latitudes (20-40˚S) and are advected eastward between South Africa and Madagascar following a wave shape (Fig. 8). Given the Australian BB aerosol are mainly located in the mid-latitudes (Fig. 4a), we can reasonably conclude that the filament reaching the SWIO basin contains aerosol from the Australian BB event. On 27th January, air masses containing aerosol are observed at Madagascar and its surroundings (Fig. 8a). These air masses are advected eastward and reach Reunion on 28th January (Fig. 8b).

Our analysis demonstrated that the Australian BB plume was transported over the SWIO basin following two distinct pathways.

4.3 Contribution of the Australian BB plume on the CO and aerosol variability

Because a significant simultaneous increase of CO and sAOD is observed over Reunion and its surroundings from 16th to 29th January 2020, the investigation will focus on this period. The emission sensitivity from FLEXPART, at the altitude where the emissions are injected is combined with CO and aerosol (BC and OC) emission inventory. The CO emissions due to anthropogenic activity are also taken into account by coupling the FLEXPART model with the EDGAR inventory information. The simulated sAOD compare fairly well with the available satellite observations during the 15-29 January period, and the peak observed on mid-January is acceptably well reproduced. Conversely, the partial column of CO seems less consistent with the observations made by IASI.

The discrepancies between FLEXPART and observations may be attributable to several possible caveats. One of which can be the lack of the vertical motion induced by pyro-convection in FLEXPART. We tested this issue by applying an injection height in agreement with CALIOP observations (9-16 km, Fig. 1) for the Australian plume (Khaykin et al., 2020). The injection height of the plume plays a key role in its long-range transport (Sofiev et al., 2012). An inappropriate or unrealistic injection height can lead to either a dilution or an overestimation of the plume. The injection height depends on the intensity of the fire, as well as on the meteorological conditions. Another possible explanation in these differences can come from the duration of the backward calculation (1 month) and an underestimation of the emission by GFAS (Brocchi et al., 2018). Using FLEXPART simulations, Brocchi et al. (2018) reveal that an amplification factor of two has been applied to CO emissions from GFAS to obtain comparable similar CO quantities with observations. The other source of difference between the model and the observations stems mainly from whether or not FLEXPART takes several regions into account as a source of pollution. The results shown in the figure 9 target emissions from Australia only. The contribution of other regions is discussed in section 5.

On average, the aerosol emissions from Australia contributed up to 95 % of the sAOD variability over Reunion from 15th to 29th January (Fig. 9a). Conversely, the CO emissions from Australia contribute up to 10% of the enhancement of the partial column of CO from 15th to 29th January (Fig. 9b). Therefore, the transport of the CO plume induced by the Australian sources has not been efficiently transported over the SWIO basin. The variability of CO over the SWIO basin in January is therefore not significantly driven by emissions from Australian fires.

5. Discussion on the influence of the regional sources

Fire Radiation Power (FRP) gives quantitative information on combustion rates and its intensity (Fig. 10a). The sparse activity of the African fires in January is clearly illustrated in Figure 11a with moderate values of FRP ranging from 20 to 200 $MW.m^{-2}$. These values are ten times lower than those observed over the southeastern Australia between 30th December 2019 and 12th January 2020 (Bègue et al., 2021). The off-season African BB activity in January 2020 is mainly located over the northwestern (near the Equator) and southeastern side of southern Africa. The most intense values (100-200 $MW.m^{-2}$) are observed over the southeastern side.

Despite this sparse activity of BB, the amount of CO injected into the atmosphere is fairly significant(from 5 to 6×10^{17} $molecules.cm^{-2}$) as shown in figure 10b. The partial column of CO (between 9 and 30 km) over southern Africa from 16th and 29th January is characterized by two regions of high values (higher than 5×10^{17} $molecules.cm^{-2}$, Fig. 10b). The first region stretches between the eastern side of southern Africa and the western side of Madagascar which corresponds to a domain extending between 10˚S and 25˚S in latitude and 30˚E and 45˚E in longitude (Fig. 10b). The second region is located on the opposite side, over a domain extending between 10˚S and 15˚S in latitude and 5˚E and 15˚E in longitude.

The main convective regions presenting negative outgoing longwave radiation anomalies, are located in mainland Africa between 12˚ S and 25˚ S and the northern side of the SWIO basin between 16th and 29th January as shown in figure 10c through observation obtained from NCEP. The daily brightness temperature values obtained from MODIS during the same period (not shown) are ranging from 195 to 210 K over the eastern side of southern Africa and the northern tip of Madagascar. These values of brightness temperature can be attributed to deep convection clouds (Héron et al., 2020; Young et al., 2013).

On average, the motion of ITCZ over the southern Africa on January is characterized by southward motion from 5˚N to 20˚S in latitude occurring between 20˚ E and 35˚ E in longitude (Fig 10a; Lashkari et al., 2017). A tropical depression formed near the northwestern side of Madagascar between 20th and 22nd January 2020. This tropical depression reached the stage of strong tropical storm on 24th January 2020 and named Diane by the RSMC (Regional Specialized Meteorological Centre) of Reunion. The intensification of the tropical depression into strong tropical storm occurred around the northern tip of Madagascar. Diane passed near Reunion on 25th January 2020 (Fig. 10c). The convective activity over southern Africa and the SWIO basin may hence be due to both ITCZ proximity and Diane activity.

To further investigate the convection driven pathway, the vertical cross section of CO and water vapor mixing ratio anomalies calculated from MLS observations between 16th to 29th January 2020 are analyzed (Figs. 11a and 11b). The CO and water vapor mixing ratio anomalies are calculated as a relative difference by considering the monthly background means as the reference values. The calculations are performed over a domain extending between 10˚S and 25˚S in latitude and 30˚E and 60˚E in longitude (black box in Fig. 10b). This domain includes both the region of deep convection and the first region of high values of CO. The monthly background is calculated from available MLS observations in January between 2017 and 2019. Figure 12a exhibits two regions of high values of CO mixing ratio anomalies (higher than 15%) centered at 37˚E and 50˚E in longitude at 146 hPa (~15 km) and 100 hPa (~17 km). These regions of CO mixing ratio anomalies are in coincidence with two regions of high values (higher than 20%) of water vapor mixing anomalies (Fig. 11b). This is consistent with the FLEXPART simulations shown in figure 12 which highlight a lift of air masses from the lower troposphere to lower stratosphere between 25°E to 55˚ E in longitude. The convective activity induced by Diane near Madagascar may have contributed to lift air masses enriched in CO from the lower troposphere.

Figure 9 also depicts the evolution of the contribution of the African emission on CO partial columns obtained from satellites observations and simulated by FLEXPART from 15th to 29th January over Reunion. An injection height ranging up to 3 km was chosen for the African fires (Labonne et al., 2007). The Australia contribution on the observed partial column was plotted again (as from figure 9). On average, the CO emissions from Africa contribute up to 90% of the enhancement of the partial column of CO from 15th to 29th January (Fig. 13b). The total Africa and Australia CO contribution reproduce fairly well the observations.

Our results suggest that the variability of CO over the SWIO basin can be explained both by the influence of the regional transport from southern Africa, enhanced by convective activity due to the passage of a tropical storm.

6. Summary and Conclusion

The complex aerosol and CO variabilities over the SWIO basin during the 2020 austral summer have been investigated. The meteorological context and the extensive fires over southeastern Australia were favorable for triggering pyro-convective events between 29th December 2019 and 12th January 2020. These pyro-convective events led to a massive injection of combustion products in the stratosphere. The ground-based and space-borne lidars revealed the presence of an intense stratospheric aerosol layer over the southeastern Australia region. Over the Lauder site in New-Zealand, this smoke layer was detected into the stratosphere (centered at 16 km) until April and beyond. The analysis of the spatial and temporal dispersion of the Australian BB plume highlighted its quick transport circling the entire Southern Hemisphere in less than two weeks. Furthermore, the satellite observations revealed that the transport of the Australian smoke layer was mainly bounded within an extra-tropical latitudinal band.

Nevertheless, the numerical models clearly showed the influence of the Australian smoke layer on the variability of aerosol over the SWIO basin. Over Reunion, the aerosol extinction profiles exhibited a significant increase in the lower stratosphere during the end of January. The MIMOSA simulations highlighted the isentropic transport of the Australian BB aerosol from extra-tropical latitudes to Reunion at 400 K isentropic level, on 28th January. As a consequence, the corresponding aerosol extinction profile exhibited a sudden increase by drawing a structure similar to a laminae at the 400 K isentropic level. The aerosol extinction profiles also exhibited a moderate increase in the upper troposphere.

According to our simulations, the CO variability over the SWIO cannot be explained by the Australian Black Summer. Rather, the CO in the UT-LS is likely driven by African BB emissions during the convective season. The analysis of satellite observations and FLEXPART simulations suggests that, because of the convective activity, air masses enriched in CO have been lifted from the lower troposphere to the lower stratosphere. Air masses from Africa contributed up to 90% of the partial column (between 9 and 30 km) of CO variability over Reunion and its surroundings. The simulations show that the modulation of the CO and aerosol extinction in the upper troposphere and the lower stratosphere over Reunion was driven by the transport of air masses from both Africa and Australia, respectively.

Acknowledgements

Data used in this publication were obtained from NDACC network and are available through its website (http://www.ndacc.org/). The work of S. Khaykin has been supported by the Agence Nationale de la Recherche PyroStrat project (21-CE01- 335 0007-01). IASI was developed and built under the responsibility of the “Centre National d’Etudes Spatiales” (CNES, France) and flown on board the MetOp satellites as part of the EUMETSAT Polar System. The authors thank the AERIS infrastructure (https://iasi.aeris-data.fr/) for providing access to the IASI data, the National Aeronautical and Space Administration (NASA) for providing CALIOP data, MLS and MODIS fire products. We would especially like to thank the staff of the team working on the lidar systems at the Maïdo observatory. The French Research Infrastructure ACTRIS-FR, CNES are also acknowledged for their support in the upgrade and operation of the Maïdo observatory lidars. Lauder observations are funded by the New-Zealand Government's Strategic Science Investment Fund (SSIF), administered by the Ministry of Business, Innovation and Employment (MBIE). The TCCON site at Réunion Island has been operated by the Royal Belgian Institute for Space Aeronomy with financial support since 2014 by the EU project

ICOS-Inwire, the ministerial decree for ICOS (FR/35/IC1 to FR/35/C6), ESFRI-FED ICOS-BE project and local activities supported by LACy/UMR8105 and by OSU-R/UMS3365 – Université de La Réunion. The lidar measurements at Lauder are supported by funding from GOSAT series project.

Data availability

The data used for this study are available and open access by request to scientist mentioned or through the link hereafter: Lidar measurements (tetsu@mri-jma.go.jp, nelson.begue@univ-reunion.fr), FTIR measurements from TCCON network (mahesh.sha@aeronomie.be); Lauder FTIR data available on the NDACC public access database (https://www-air.larc.nasa.gov/missions/ndacc/data.html); The satellite observations and emission inventory used are available on-line from the sources as stated in the manuscript. The FLEXPART and MIMOSA codes are available on the FLEXPART (https://www.flexpart.eu/) and AERIS website (http://espri.aeris-data.fr/), respectively.

Authors contributions

Conceptualization, N.B.; methodology and software, N.B, A.B. and G.K.; validation and data curation, N.B., A.B, GK., S.K, C.C., P.C., D.S., J.R., R.Q, B.R, S.T and P.S.; original draft preparation and writing, N.B.; The FLEXPART and MIMOSA simulations have been performed by GK and NB, respectively. All authors have read and agreed to the published version of the manuscript.

REFRENCES

Aliaga, D., Sinclair, V. A., Andrade, M., Artaxo, P., Carbone, S., Kadantsev, E and Bianchi, F.: Identifying source regions of air masses sampled at the tropical high-altitude site of Chacaltaya using WRF-FLEXPART and cluster analysis. Atmospheric Chemistry and Physics, 21(21), 16453-16477, 2021

Andreae, M. O and Merlet, P.: Emission of trace gases and aerosols from biomass burning. Global biogeochemical cycles, 15(4), 955-966, 2001

Atkinson, R., Baulch, D. L., Cox, R. A., Crowley, J. N., Hampson, R. F., Hynes, R. G., Jenkin, M. E., Rossi, M. J., Troe, J., and IUPAC Subcommittee: Evaluated kinetic and photochemical data for atmospheric chemistry: Volume II – gas phase reactions of organic species, Atmos. Chem. Phys., 6, 3625–4055, https://doi.org/10.5194/acp-6-3625-2006, 2006.

Baray, J.-L., Courcoux, Y., Keckhut, P., Portafaix, T., Tulet, P., Cammas, J.-P., Hauchecorne, A., Godin Beekmann, S., De Mazière, M., Hermans, C., Desmet, F., Sellegri, K., Colomb, A., Ramonet, M., Sciare, J., Vuillemin, C., Hoareau, C., Dionisi, D., Duflot, V., Vérèmes, H., Porteneuve, J., Gabarrot, F., Gaudo, T., Metzger, J.-M., Payen, G., Leclair de Bellevue, J., Barthe, C., Posny, F., Ricaud, P., Abchiche, A., and Delmas, R.: Maïdo observatory: a new high-altitude station facility at Reunion Island (21° S, 55° E) for long-term atmospheric remote sensing and in situ measurements, Atmos. Meas. Tech., 6, 2865–2877, https://doi.org/10.5194/amt-6-2865-2013, 2013

Baray, J.-L., Leveau, J., Baldy, S., Jouzel, J., Keckhut, P., Bergametti, G., Ancellet, G., Bencherif, H., Cadet, B., Carleer, M., David, C., De Mazière, M., Faduilhe, D., Godin-Beekmann, S., Goloub, P., Goutail, F., Metzger, J.-M., Morel, B., Pommereau, J.-P., Porteneuve, J., Portafaix, T., Posny, F., ROBERT, L., and Van Roozendael, M.: An instrumented station for the survey of ozone and climate change in the southern tropics, 8, 1020–1028, https://doi.org/10.1039/b607762e, 2006.

Barimalala, R., Desbiolles, F., Blamey, R. C., & Reason, C.: Madagascar influence on the South Indian Ocean Convergence Zone, the Mozambique Channel Trough and southern African rainfall. Geophysical Research Letters, 45, 11,380–11,389. https://doi.org/10.1029/2018GL079964, 2018

Baron, A., Chazette, P., Khaykin, S., Payen, G., Marquestaut, N., Bègue, N. and Duflot, V. (2023). Early Evolution of the Stratospheric Aerosol Plume Following the 2022 Hunga Tonga-Hunga Ha'apai Eruption: Lidar Observations From Reunion (21° S, 55° E). Geophysical Research Letters, 50(10), https://doi.org/10.1029/2022GL101751, e2022GL101751.

Barthe, C., Bousquet, O., Bielli, S., Tulet, P., Pianezze, J., Claeys, M. and Zucule, J.: Impact of tropical cyclones on inhabited areas of the swio basin at present and future horizons. part 2: Modeling component of the research program renovrisk-cyclone. Atmosphere, 12(6), 689, 2021

Bègue, N., Bencherif, H., Jegou, F., Vérèmes, H., Khaykin, S., Krysztofiak, G., Portafaix, T., Duflot, V., Baron, A., Berthet, G., Kloss, C., Payen, G., Keckhut, P., Coheur, P-F., Clerbeaux, C., Smale, D., Robinson, J., Querel, R and Smale, P. : Transport and variability of tropospheric ozone over Oceania and southern pacific during the 2019–20 Australian bushfires. Remote Sensing, 13(16), 3092, 2021

Bègue, N., Vignelles, D., Berthet, G., Portafaix, T., Payen, G., Jégou, F., Bencherif, H., Jumelet, J., Vernier, J. P., Lurton., T., Renard, J. B., Clarisse., L., Duverger, V., Posny, F., Metzger, J. M., and Godin-Beekmann, S.: Long-range isentropic transport of stratospheric aerosols over Southern Hemisphere following the Calbuco eruption in April 2015, 15019–15036, https://doi.org/10.5194/acp-17-15019-2017, 2017.

Bencherif, H., Bègue, N., Kirsch Pinheiro, D., Du Preez, D. J., Cadet, J. M., da Silva Lopes, F. J. and Clerbaux, C.: Investigating the long-range transport of aerosol plumes following the Amazon fires (August 2019): a multi-instrumental approach from ground-based and satellite observations. Remote Sensing, 12(22), 3846, 2020

Bencherif, H., El Amraoui, L., Kirgis, G., Leclair De Bellevue, J., Hauchecorne, A., Mzé, N., Portafaix, T., Pazmino, A., and Goutail, F.: Analysis of a rapid increase of stratospheric ozone during late austral summer 2008 over Kerguelen (49.4° S, 70.3° E), Atmos. Chem. Phys., 11, 363–373, https://doi.org/10.5194/acp-11-363-2011, 2011

Boers, R., A. T. de Laat, D. C. Stein Zweers, and R. J. Dirksen: Lifting potential of solar-heated aerosol layers, Geophys. Res. Lett., 37, L24802, doi:10.1029/2010GL045171, 2010

Burton, S.P., Hair, J.W., Kahnert, M., Ferrare, R.A., Hostetler, C.A., Cook, A.L., Harper, D.B., Berkoff, T.A., Seaman, S.T., Collins, J.E., Fenn, M.A., Rogers, R.R., 2015. Observations of the spectral dependence of linear particle depolarization ratio of aerosols using NASA Langley airborne High Spectral Resolution Lidar. Atmos. Chem. Phys. 15, 13453–13473. https://doi.org/10.5194/acp-15-13453-2015

Brasseur, G. and Solomon, S: Aeronomy of the Middle Atmosphere: Chemistry and Physics of the Stratosphere and Mesosphere, 3rd edn, 644, Springer-Verlag, 2005.

Cai, D., Abram, N. J., Sharples, J. J. and Perkins-Kirkpatrick, S. E. (2022). Increasing intensity and frequency of cold fronts contributed to Australia's 2019–2020 Black Summer fire disaster. Environmental Research Letters, 17(9), 094044.

Campanelli, M., Estelles, V., Tomasi, C., Nakajima, T., Malvestuto, V., and Martinez-Lozano, J. A.: Application of the SKYRAD improved Langley plot method for the in-situ calibration of CIMEL sun-sky photometers, Appl. Optics, 46, 2688–2702, 2007.

Che, H., Shi, G., Uchiyama, A., Yamazaki, A., Chen, H., Goloub, P., and Zhang, X.: Intercomparison between aerosol optical properties by a PREDE skyradiometer and CIMEL sunphotometer over Beijing, China, Atmos. Chem. Phys., 8, 3199–3214, doi:10.5194/acp-8-3199-2008, 2008.

Clain, G., Baray, J. L., Delmas, R., Diab, R., Leclair de Bellevue, J., Keckhut, P., Posny, F., Metzger, J. M., and Cammas, J. P.: Tropospheric ozone climatology at two Southern Hemisphere tropical/subtropical sites, (Reunion Island and Irene, South Africa) from ozonesondes, LIDAR, and in situ aircraft measurements, 9, Atmos. Chem. Phys., 1723–1734, https://doi.org/10.5194/acp-9-1723-2009, 2009

Clerbaux, C., Boynard, A., Clarisse, L., George, M., Hadji-Lazaro, J., Herbin, H., Hurtmans, D., Pommier, M., Razavi, A., Turquety, S: Monitoring of atmospheric composition using the thermal infrared IASI/MetOp sounder, Atmos. Chem. Phys. 2009, 9, 6041–6054, 2009.

Coheur, P.-F., Clarisse, L., Turquety, S., Hurtmans, D., and Clerbaux, C.: IASI measurements of reactive trace species in BB plumes, Atmos. Chem. Phys., 9, 5655–5667, doi:10.5194/acp-9-5655-2009, 2009.

Darbyshire, E., Morgan, W. T., Allan, J. D., Liu, D., Flynn, M. J., Dorsey, J. R and Coe, H: The vertical distribution of biomass burning pollution over tropical South America from aircraft in situ measurements during SAMBBA. Atmospheric Chemistry and Physics, 19(9), 5771-5790, 2019

De Laat, A.T.J.; Stein Zweers, D.C.; Boers, R.; Tuinder, O.N. A solar escalator: Observational evidence of the self-lifting of smoke and aerosols by absorption of solar radiation in the February 2009 Australian Black Saturday plume. J. Geophys. Res. Atmos. 2012, 117.

Dowdy, A. J and Pepler, A: Pyroconvection risk in Australia: Climatological changes in atmospheric stability and surface fire weather conditions. Geophysical Research Letters, 45, 2005–2013. https://doi.org/10.1002/2017GL076654, 2018

De Mazière, M., Sha, M. K., Desmet, F., Hermans, C., Scolas, F., Kumps, N., Metzger, J.-M., Duflot, V., and Cammas, J.-P.: TCOON data from Réunion Island 5RE), Release GG2014.R1, Version R1, CaltechDATA [data set], https://doi.org/10.14291/TCCON.GGG2014.REUNION01.R1, 2017

Duflot, V., Dils, B., Baray, J. L., De Mazière, M., Attié, J. L., Vanhaelewyn, G and Delmas, R.: Analysis of the origin of the distribution of CO in the subtropical southern Indian Ocean in 2007. Journal of Geophysical Research: Atmospheres, 115(D22), 2010

Duflot, V., Bègue, N., Pouliquen, M. L., Goloub, P. and Metzger, J. M : Aerosols on the Tropical Island of La Réunion (21° S, 55° E): Assessment of Climatology, Origin of Variability and Trend. Remote Sensing, 14(19), 4945, 2022

Eckhardt, S., Cassiani, M., Evangeliou, N., Sollum, E., Pisso, I., and Stohl, A.: Source–receptor matrix calculation for deposited mass with the Lagrangian particle dispersion model FLEXPART v10.2 in backward mode, Geosci. Model Dev., 10, 4605–4618, https://doi.org/10.5194/gmd-10-4605-2017, 2017.

Edwards, D. P., Emmons, L. K., Gille, J. C., Chu, A., Attié, J. L., Giglio, L and Drummond, J. R.: Satellite-observed pollution from Southern Hemisphere biomass burning. Journal of Geophysical Research: Atmospheres, 111(D14), 2006

Forster, C., Stohl, A., and Seibert, P.: Parameterization of convective transport in a Lagrangian particle dispersion model and its evaluation, J. Appl. Meteorol. Clim., 46, 403–422, 2007.

Fromm, M., Lindsey, D. T., Servranckx, R., Yue, G., Trickl, T., Sica, R.: The untold story of pyro-cumulonimbus. Bulletin of the American Meteorological Society, 91(9), 2010

Hamill, P., Jensen, E. J., Russell, P. B., and Bauman, J. J.: The life cycle of stratospheric aerosol particles, B. Am. Meteorol. Soc., 78, 1395–1410, https://doi.org/10.1175/1520-0477(1997)078E2.0.CO;2, 1997

Garstang, M., Tyson, P. D., Browell, E. and Swap, R. J.: . Large scale transport of biogenic and biomass burning products. JS Levine, 389-395, 1996

Grythe, H., Kristiansen, N. I., Groot Zwaaftink, C. D., Eckhardt, S., Ström, J., Tunved, P., Krejci, R., and Stohl, A.: A new aerosol wet removal scheme for the Lagrangian particle model FLEXPART v10, Geosci. Model Dev., 10, 1447–1466, https://doi.org/10.5194/gmd-10-1447-2017, 2017.

Haarig, M.; Ansmann, A.; Baars, H.; Jimenez, C.; Veselovskii, I.; Engelmann, R.; Althausen, D. Depolarization and lidar ratios at 355, 532, and 1064 nm and microphysical properties of aged tropospheric and stratospheric Canadian wildfire smoke. Atmos. Chem. Phys. 2018, 18, 11847–11861.

Hashimoto, M., Nakajima, T., Dubovik, O., Campanelli, M., Che, H., Khatri, P., Takamura, T and Pandithurai, G: Development of a new data-processing method for SKYNET sky radiometer observations. Atmospheric Measurement Techniques, 5(11), 2723-2737, 2012

Hauchecorne, A., Godin, S., Marchand, M., Heese, B., and Souprayen, C.: Quantification of the transport of chemical constituents from the polar vortex to midlatitudes in the lower stratosphere using the high-resolution advection model MIMOSA and effective diffusivity, J. Geophys. Res.-Atmos., 107, 1–13, 2002

Héron, D., Evan, S., Brioude, J., Rosenlof, K., Posny, F., Metzger, J. M., & Cammas, J. P.: Impact of convection on the upper-tropospheric composition (water vapor and ozone) over a subtropical site (Réunion island; 21.1° S, 55.5° E) in the Indian Ocean. Atmospheric Chemistry and Physics, 20(14), 8611-8626., 2020

Heese, B., Godin, S., and Hauchecorne, A.: Airborne lidar measurements of ozone filaments during METRO–A validation of PV advection model MIMOSA, J. Geophys. Res, 106, 20011–20024, 2001.

Holanda, B. A., Pöhlker, M. L., Walter, D., Saturno, J., Sörgel, M., Ditas, J and Pöhlker, C: Influx of African biomass burning aerosol during the Amazonian dry season through layered transatlantic transport of black carbon-rich smoke. Atmospheric Chemistry and Physics, 20(8), 4757-4785, 2020

Hu, Q., Goloub, P., Veselovskii, I., Bravo-Aranda, J.-A., Popovici, I. E., Podvin, T., Haeffelin, M., Lopatin, A., Dubovik, O., Pietras, C., Huang, X., Torres, B., and Chen, C.: Long-range-transported Canadian smoke plumes in the lower stratosphere over northern France, Atmos. Chem. Phys., 19, 1173–1193, https://doi.org/10.5194/acp-19-1173-2019, 2019.

Hurtmans, D., Coheur, P.F.; Wespes, C., Clarisse, L., Scharf, O., Clerbaux, C., Hadji-Lazaro, J., George, M., Turquety, S: FORLI radiative transfer and retrieval code for IASI. J. Quant. Spectrosc. Radiat. Transf. 2012, 113, 1391–1408, 2012

Jäger, H. and Deshler, T.: Lidar backscatter to extinction, mass and area conversions for stratospheric aerosols based on midlatitude balloon borne size distribution measurements, Geophys. Res. Lett., 29, 1929, https://doi.org/10.1029/2002GL015609, 2002

Jones, N. B., Rinsland, C. P., Liley, J. B., and Rosen, J.: Correlation of aerosol and carbon monoxide at 45 S: Evidence of BB emissions. Geophysical research letters, 28(4), 709-712., 2001

Kablick III, G. P., Allen, D. R., Fromm, M. D. and Nedoluha, G. E: Australian pyroCb smoke generates synoptic-scale stratospheric anticyclones, Geophys. Res. Let., 47(13), e2020GL088101, 2020.

Khaykin, S., Legras, B., Bucci, S., Sellitto, P., Isaksen, L., Tence, F. and Godin-Beekmann, S: The 2019/20 Australian wildfires generated a persistent smoke-charged vortex rising up to 35 km altitude. Communications Earth & Environment, 1(1), 1-12, 2020.

Khaykin, S. M., Godin-Beekmann, S., Hauchecorne, A., Pelon, J., Ravetta, F., and Keckhut, P: Stratospheric smoke with unprecedentedly high backscatter observed by lidars above southern France, Geophys. Res. Lett., 1944, 8007, doi:10.1002/2017GL076763, 2018.

Kaufman, Y. J., Ichoku, C., Giglio, L., Korontzi, S., Chu, D. A., Hao, W. M and Justice, C. O.: Fire and smoke observed from the Earth Observing System MODIS instrument--products, validation, and operational use. International Journal of Remote Sensing, 24(8), 1765-1781, 2003

Klett, J. D.: Lidar inversion with variable backscatter/extinction ratios, Appl. Opt., AO, 24, 1638–1643, https://doi.org/10.1364/AO.24.001638, 1985.

Kloss, C.; Sellitto, P., Von Hobe, M.; Berthet, G.; Smale, D.; Krysztofiak, G.; Legras, B. Australian fires 2019–2020: Tropospheric and stratospheric pollution throughout the whole fire season. Front. Environ. Sci. 2021, 9, 220, 2021

Kloss, C., Berthet, G., Sellitto, P., Ploeger, F., Bucci, S., Khaykin, S., Jégou, F., Taha, G., Thomason, L. W., Barret, B., Le Flochmoen, E., von Hobe, M., Bossolasco, A., Bègue, N., and Legras, B.: Transport of the 2017 Canadian wildfire plume to the tropics via the Asian monsoon circulation, Atmos. Chem. Phys., 19, 13547–13567, https://doi.org/10.5194/acp-19-13547-2019, 2019.

Kremser, S., Thomason, L. W., Hobe, M., et al.: Stratospheric aerosol – Observations, processes, and impact on climate, Rev. Geophys., 54, 278–335, 2016.

Labonne, M., Bréon, F. M., & Chevallier, F. : Injection height of biomass burning aerosols as seen from a spaceborne lidar. *Geophysical research letters*, *34*(11)., 2007

Lashkari, H., Mohammadi, Z., and Keikhosravi, G.: Annual fluctuations and displacements of inter tropical convergence zone (ITCZ) within the range of Atlantic Ocean-India. Open Journal of Ecology, 7(1), 12-33, 2017

Levin, N., Yebra, M. and Phinn, S.: Unveiling the factors responsible for Australia's Black Summer fires of 2019/2020. Fire, 4(3), 58, 2021

Livesey, N. J., Read, W. G., Wagner, P. A., Froidevaux, L., Santee, M. L., Schwartz, M. J., Lambert, A., Valle, L. F. M., Pumphrey, H. C., Manney, G. L., Fuller, R. A., Jarnot, R. F., Knosp, B. W., and Lay, R. R.: Version 5.0x Level 2 and 3 data quality and description document., https://mls.jpl.nasa.gov/data/v5-0_data_quality_document.pdf, 2022.

de Mazière, M. D., Thompson, A. M., Kurylo, M. J., Wild, J. D., Bernhard, G., Blumenstock, T. and Strahan, S. E: The Network for the Detection of Atmospheric Composition Change (NDACC): history, status and perspectives, Atmos. Chem. Phys., 18(7), 4935-4964, 2018

Morgan, W. T., Allan, J. D., Bauguitte, S., Darbyshire, E., Flynn, M. J., Lee, J and Coe, H: Transformation and aging of biomass burning carbonaceous aerosol over tropical South America from aircraft in-situ measurements during SAMBBA, 2019

Müller, D., Ansmann, A., Mattis, I., Tesche, M., Wandinger, U., Althausen, D., and Pisani, G.: Aerosol-type-dependent lidar ratios observed with Raman lidar, J. Geophys. Res., 112, D16202, https://doi.org/10.1029/2006JD008292, 2007

Nakajima, T., Tonna, G., Rao, R., Kaufman, Y., and Holben, B.: Use of sky brightness measurements from ground for remote sensing of particulate polydispersions. Appl. Optics, 35, 2672–2686, 1996

Neumann, C.: Global guide to tropical cyclone forecasting, WMO Trop. Cyclone Program Rep. TCP-31, chap. Global Overview, World Meteorol. Organ., Geneva, Switzerland, 43 pp., 1993

Nicolae, D., Nemuc, A., Müller, D., Talianu, C., Vasilescu, J., Belegante, L. and Kolgotin, A. : Characterization of fresh and aged BB events using multiwavelength Raman lidar and mass spectrometry. Journal of Geophysical Research: Atmospheres, 118(7), 2956-2965, 2013

Ohneiser, K., Ansmann, A., Kaifler, B., Chudnovsky, A., Barja, B., Knopf, D. A and Zamorano, F.: Australian wildfire smoke in the stratosphere: the decay phase in 2020/2021 and impact on ozone depletion. Atmospheric Chemistry and Physics, 22(11), 7417, 2022

Ohneiser, K., Ansmann, A., Baars, H., Seifert, P., Barja, B., Jimenez, C and Wandinger, U.: Smoke of extreme Australian bushfires observed in the stratosphere over Punta Arenas, Chile, in January 2020: optical thickness, lidar ratios, and depolarization ratios at 355 and 532 nm. Atmospheric Chemistry and Physics, 20(13), 8003-8015, 2020

Pisso, I., Sollum, E., Grythe, H., Kristiansen, N. I., Cassiani, M., Eckhardt, S., Arnold, D., Morton, D., Thompson, R. L., Groot Zwaaftink, C. D., Evangeliou, N., Sodemann, H., Haimberger, L., Henne, S., Brunner, D., Burkhart, J. F., Fouilloux, A., Brioude, J., Philipp, A., Seibert, P., and Stohl, A.: The Lagrangian particle dispersion model FLEXPART version 10.4, Geosci. Model Dev., 12, 4955–4997, https://doi.org/10.5194/gmd-12-4955-2019, 2019.

Portafaix, T., Morel, B., Bencherif, H., Baldy, S., Godin-Beekmann, S., and Hauchecorne, A.: Fine-scale study of a thick stratospheric ozone lamina at the edge of the southern subtropical barrier, J. Geophys. Res.-Atmos., 108, D64196, https://doi.org/10.1029/2002JD002741, 2003.

Pumphrey, H. C., Filipiak, M. J., Livesey, J., Scwartz, M. J., Boone, C., Walker, K. A., Bernath, P., Ricaud, P., Barret, B., Clerbaux, C., Jarnot, R. F., Manney, G. L. and Waters, J. W: Validation of middle-atmosphere carbon monoxide retrievals from the Microwave Limb Sounder on Aura, J. Geophys. Res., 112, D24S38, doi: 10.1029/2007JD008723, 2007.

Russell-Smith, J.; Yates, C.P.; Whitehead, P.J.; Smith, R.; Craig, R.; Allan, G.E.; Thackway, R.; Frakes, I.; Cridland, S.;Meyer, M.C.P.; et al. Bushfires' down under': Patterns and implications of contemporary Australian landscape burning. Int. J.Wildland Fire, 16, 361–377, 2007

Sakai, T., T. Nagai, M. Nakazato, Y. Mano, and T. Matsumura: Ice clouds and Asian dust studied with lidar measurements of particle extinction-to-backscatter ratio, particle depolarization, and water vapor mixing ration over Tsukuba. Applied Optics 42 7103 –7116, 2003

Sakai, T., O. Uchino, T. Nagai, B. Liley, I. Morino, and T. Fujimoto: Long-term variation of stratospheric aerosols observed with lidars over Tsukuba, Japan, from 1982 and Lauder, New Zealand, from 1992 to 2015, J. Geophys. Res. Atmos., 121, 10,283–10,293, doi:10.1002/2016JD025132, 2016

Santee, M. L., Lambert, A., Manney, G. L., Livesey, N. J., Froidevaux, L., Neu, J. L. and Ward, B. M: Prolonged and pervasive perturbations in the composition of the Southern Hemisphere midlatitude lower stratosphere from the Australian New Year's fires. Geophysical Research Letters, 49(4), e2021GL096270, 2022

Schwartz, M. J., Santee, M. L., Pumphrey, H. C., Manney, G. L., Lambert, A., Livesey, N. J., and Werner, F: Australian new year's pyrocb impact on stratospheric composition. Geophysical

Research Letters, 47(24), e2020GL090831, 2020

Schoeberl, M. R., Douglass, A. R., Hilsenrath, E., Bhartia, P. K.,Barnett, J., Beer, R., Waters, J., Gunson, M., Froidevaux, L.,Gille, J., Levelt, P. F., and DeCola, P.: Overview of the EOS Aura Mission, IEEE Trans. Geosci. Remote Sens., 44, 1066–1074, 2006.

Seibert, P. and Frank, A.: Source-receptor matrix calculation with a Lagrangian particle dispersion model in backward mode, Atmos. Chem. Phys., 4, 51–63, https://doi.org/10.5194/acp-4-51-2004, 2004.

Sofiev, M., Ermakova, T. and Vankevich, R.: Evaluation of the smoke-injection height from wild-land fires using remote-sensing data. Atmospheric Chemistry and Physics, 12(4), 1995-2006, 2012

Solomon, S., Stone, K., Yu, P., Murphy, D. M., Kinnison, D., Ravishankara, A. R and Wang, P: Chlorine activation and enhanced ozone depletion induced by wildfire aerosol, Nature, 615(7951), 259-264, 2023

Stohl, A., Forster, C., Eckhardt, S., Spichtinger, N., Huntrieser, H., Heland, J., Schlager, H., Wilhelm, S., Arnold, F., and Cooper, O.: A backward modeling study of intercontinental pollution transport using aircraft measurements, J. Geophys. Res., 108, 4370, https://doi.org/10.1029/2002JD002862, 2003.

Swap, R. J., Annegarn, H. J., Suttles, J. T., King, M. D., Platnick, S., Privette, J. L and Scholes, R. J: Africa burning: a thematic analysis of the Southern African Regional Science Initiative (SAFARI 2000). Journal of Geophysical Research: Atmospheres, 108(D13), 2003

Taha, G., Loughman, R., Zhu, T., Thomason, L., Kar, J., Rieger, L. and Bourassa, A: OMPS LP Version 2.0 multi-wavelength aerosol extinction coefficient retrieval algorithm., Atmospheric Measurement Techniques, 14(2), 1015-1036, 2021

Tencé, F., Jumelet, J., Bekki, S., Khaykin, S., Sarkissian, A. and Keckhut, P.: Australian Black Summer smoke observed by lidar at the French Antarctic station Dumont d'Urville. Journal of Geophysical Research: Atmospheres, 127(4), e2021JD035349, 2022

Turquety, S., Menut, L., Siour, G., Mailler, S., Hadji-Lazaro, J., George, M., Clerbaux, C., Hurtmans, D., Coheur, P.-F: APIFLAME v2.0 BB emissions model: Impact of refined input parameters on atmospheric concentration in Portugal in summer 2016. Geosci. Model. Dev., 2020, 13, 2981–3009, 2020.

Uchino, O., Tokunaga, M., Seki, K., Maeda, M., Naito, K., and Takahashi, K: Lidar measurement of stratospheric transmission at a wavelength of 340 nm after the eruption of El Chichon, J. Atmos. Terr. Phys., 45, 12, 849–850, 1983

Vernier, J. P., Pommereau, J. P., Garnier, A., Pelon, J., Larsen, N., Nielsen, J., and McDermid, I. S., Tropical stratospheric aerosol layer from CALIPSO lidar observations, J. Geophys. Res.-Atmos., 114, D00H10, https://doi.org/10.1029/2009JD011946, 2009

Wunch, D., Toon, G. C., Sherlock, V., Deutscher, N. M., Liu, C., Feist, D. G., and Wennberg, P. O.: The Total Carbon Column Observing Network's GGG2014 Data Version, p. 43, https://doi.org/10.14291/tccon.ggg2014.documentation.R0/122, 2015.

Young, S.A.: Analysis of lidar backscatter profiles in optically thin clouds, Appl. Opt., 34, 7019–7031., 1995

Xu, Y., Wang, W., Chen, B., Chang, M., & Wang, X.: Identification of ventilation corridors using backward trajectory simulations in Beijing. Sustainable Cities and Society, 70, 102889, 2021

Yu, P.; Davis, S.M.; Toon, O.B.; Portmann, R.W.; Bardeen, C.G.; Barnes, J.E.; Telg, H.; Maloney, C.; Rosenlof, K.H. Persistent Stratospheric Warming due to 2019–2020 Australian Wildfire Smoke. Geophys. Res. Lett. 2020, 2020, e2021GL092609, 2020

Yu, P., Davis, S. M., Toon, O. B., Portmann, R. W., Bardeen, C. G., Barnes, J. E and Rosenlof, K. H: Persistent stratospheric warming due to 2019–2020 Australian wildfire smoke. Geophysical Research Letters, 48(7), e2021GL092609, 2021

Zhou, M., Langerock, B., Vigouroux, C., Sha, M. K., Ramonet, M., Delmotte, M., ... & De Mazière, M.: Atmospheric CO and CH 4 time series and seasonal variations on Reunion Island from ground-based in situ and FTIR (NDACC and TCCON) measurements. Atmospheric Chemistry and Physics, 18(19), 13881-13901, 2018

FIGURES

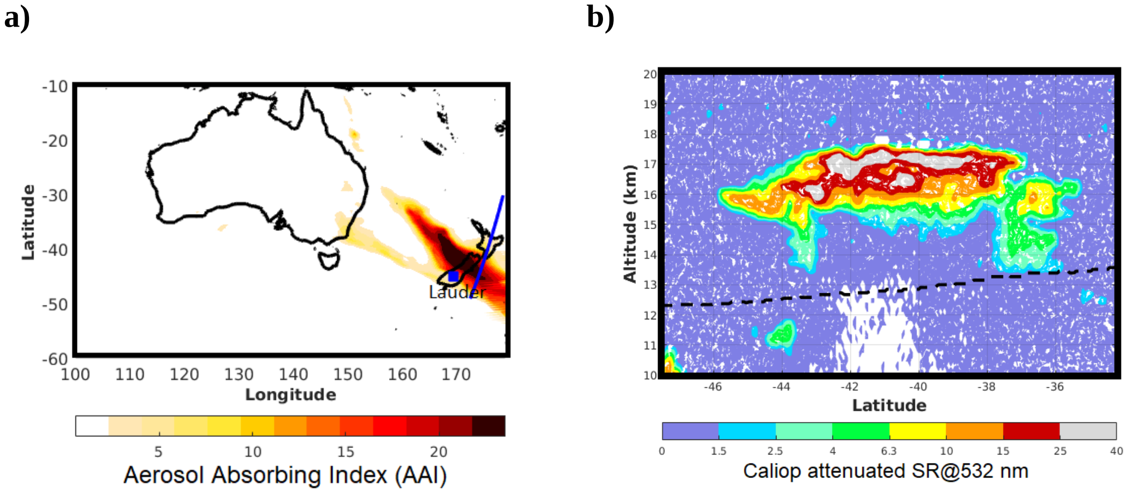

Figure 1: **(a)** Map of Aerosol Absorbing Index obtained from OMPS observations and **(b)** scattering ratio profiles at 532 nm obtained from CALIOP observations on 1st January 2020. The orbit overpass of CALIOP is indicated by the blue curve, while the blue square corresponds to the Lauder site in plot (a). The black dashed line in (b) corresponds to the 380 K isentropic level calculated from CALIOP observations.

a)

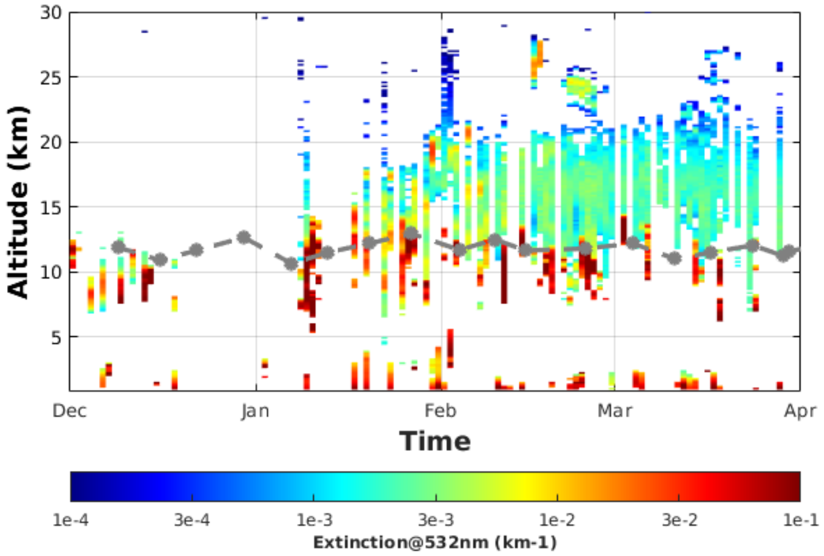

b)

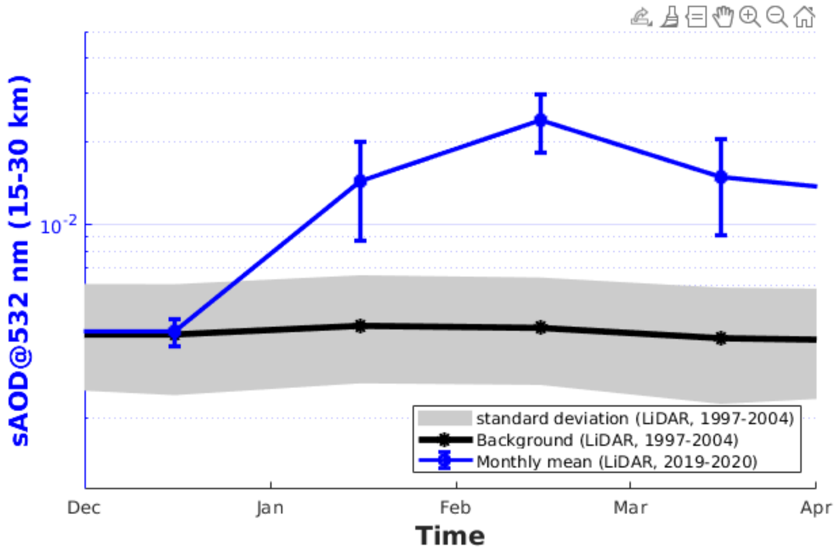

Figure 2: Time series of (a) daily profiles of aerosol extinction and (b) monthly mean of stratospheric AOD (sAOD between 15 and 30 km) at 532 nm obtained from lidar observations between 1st December 2019 and 1st April 2020. In order to screen non-aerosol contributors (such as clouds) to the extinction measurements, a mask based on the method reported by Nicolae et al. (2013), which includes consideration of plausible aerosols properties, was used. Specifically, we only kept profile parts with positive depolarization values, and Angström exponent ranges from 0.1 to 4. The grey line indicates the tropopause height obtained from radiosonde measurements. The background evolution of aerosol data and the associated standard deviation are given in black lines and grey areas, respectively.

a)

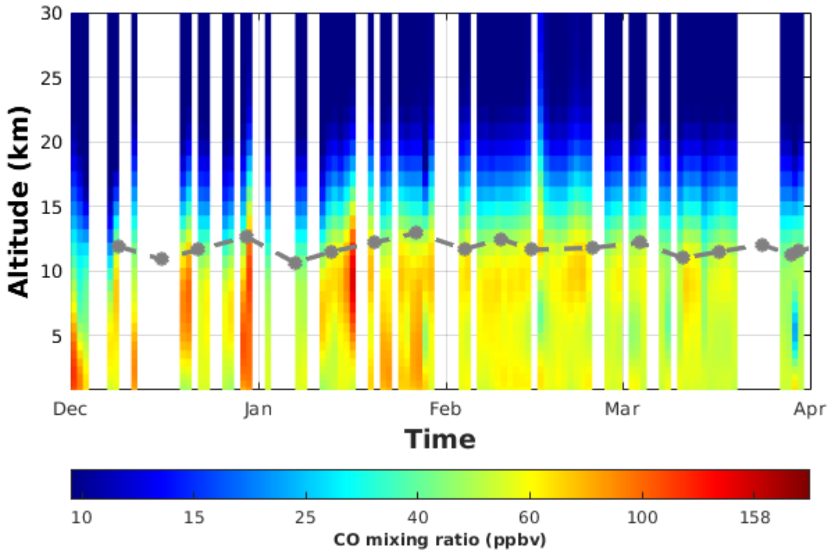

b)

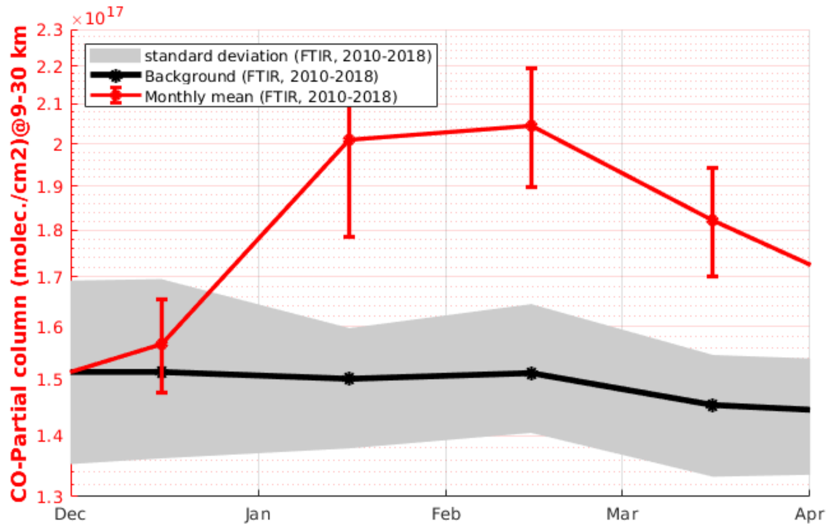

Figure 3: Time series of (a) daily profiles of CO mixing ratio and (b) monthly mean of partial column of CO (between 9 and 30 km) obtained from FTIR at Lauder between 1st December 2019 and 1st April 2020. The background evolution of the partial column of CO and the associated standard deviation are given in black lines and grey areas, respectively. .

a)

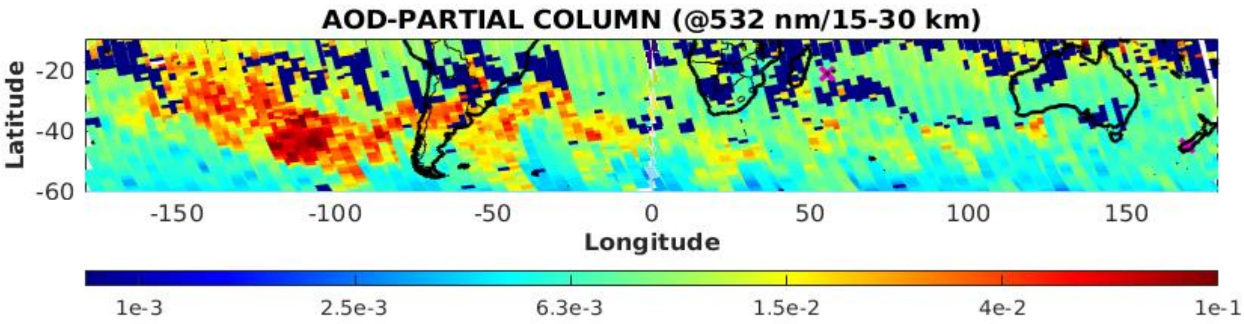

b)

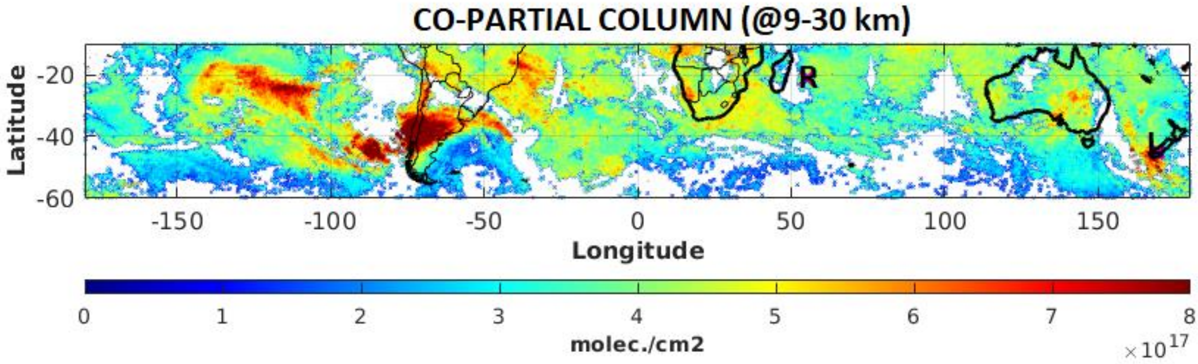

Figure 4: Time-averaged map (from 9th to 16th January 2020) of (a) sAOD (between 15 and 30 km at 532 nm) obtained from OMPS observations (b) partial column of CO (averaged between 9 and 30 km) obtained from IASI observations. The location of Reunion and Lauder sites are indicated by R and L respectively.

a)

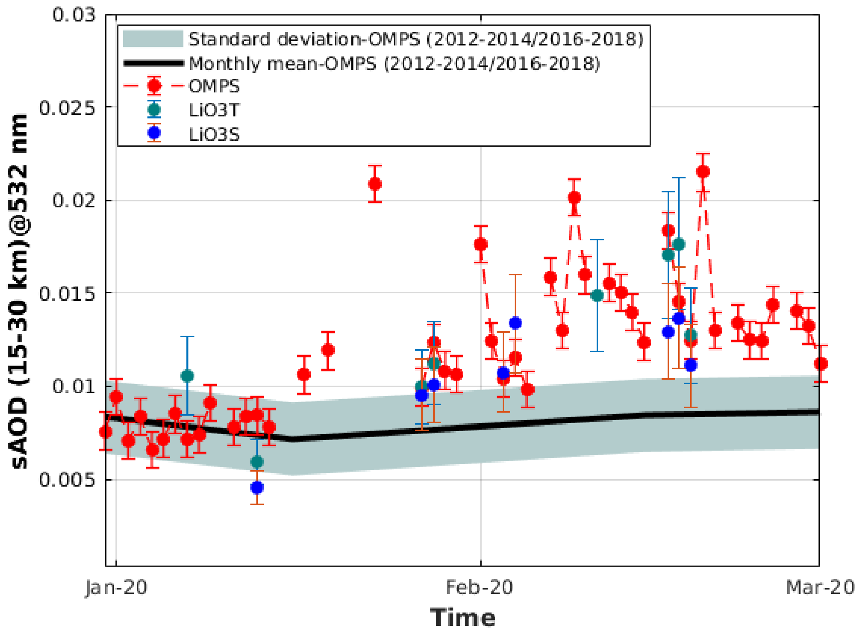

b)

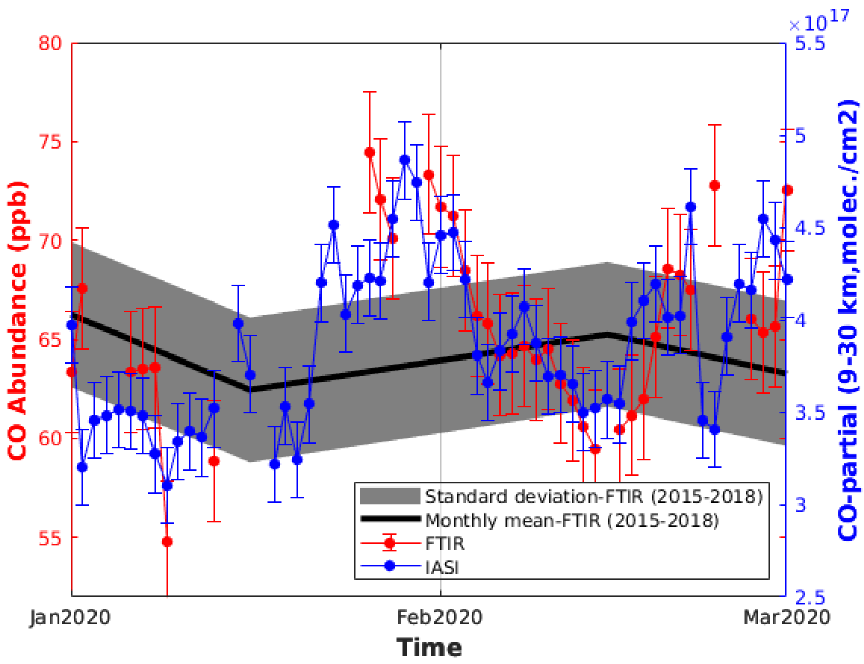

Figure 5: Daily mean evolution of aerosol (a) and CO (b) abundances obtained from ground-based and satellite observations at Reunion between 1st January and 1st March 2020. Partial column (molecule.cm^{-2}) and abundance (ppb) of CO obtained from IASI (blue line) and FTIR (red line) respectively are given in the lower panel (b), while sAOD obtained from OMPS (red line) and Lidar (blue and green dots) are given in the upper panel (a). The black and dashed lines correspond to monthly mean and the associated standard deviation calculated during the background period.

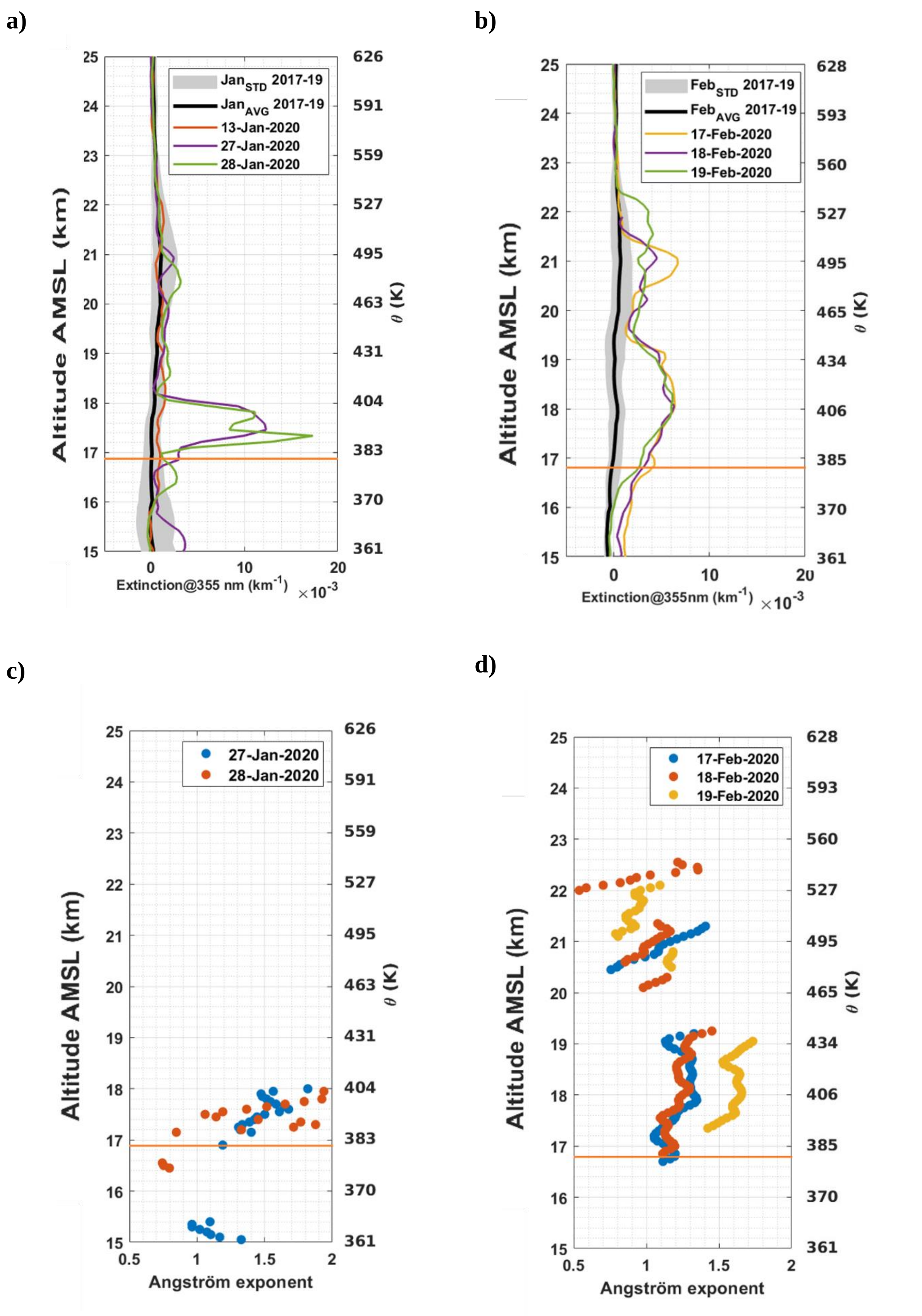

Figure 6: Aerosol extinction (at 355 nm) (a, b) and Angström exponent (355-532 nm) (c, d) obtained from lidar observations at Reunion in the months January and February 2020. The tropopause height is indicated by the orange horizontal lines.

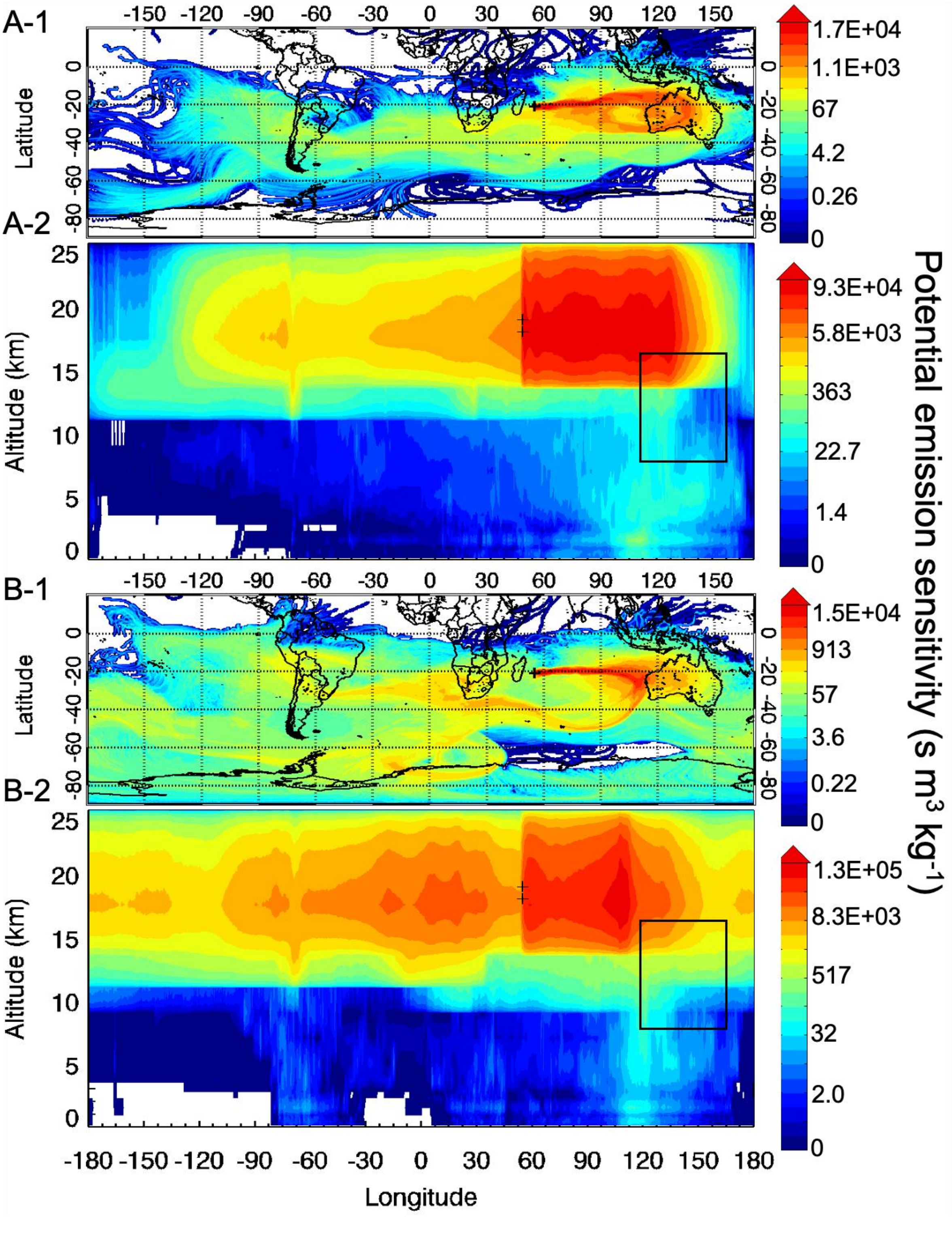

Figure 7: FLEXPART 30-day back trajectories initialized from Reunion (black cross) at 18 km on 27th January 2020 (A-1-2) and 28th January 2020 (B-1-2). A-1 and B-1 correspond to an integration of the trajectory positions over the whole altitude range. A-2 and B-2 are the vertical view integrated over the whole latitude range of the back trajectories A-1 and B-1. The black rectangle represented the injection height of the biomass burning aerosols.

a)

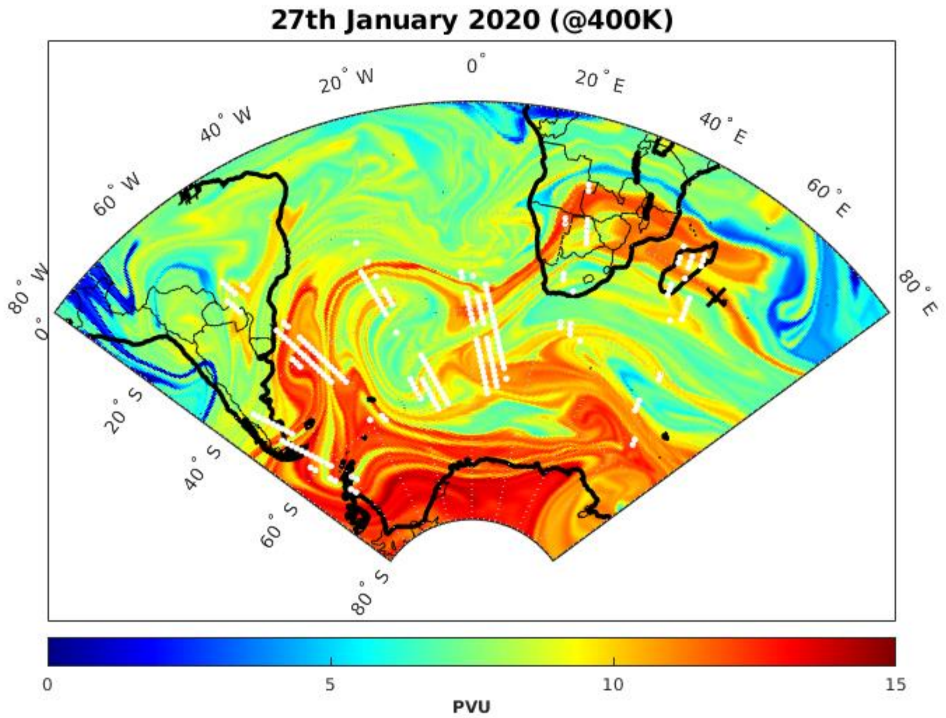

b)

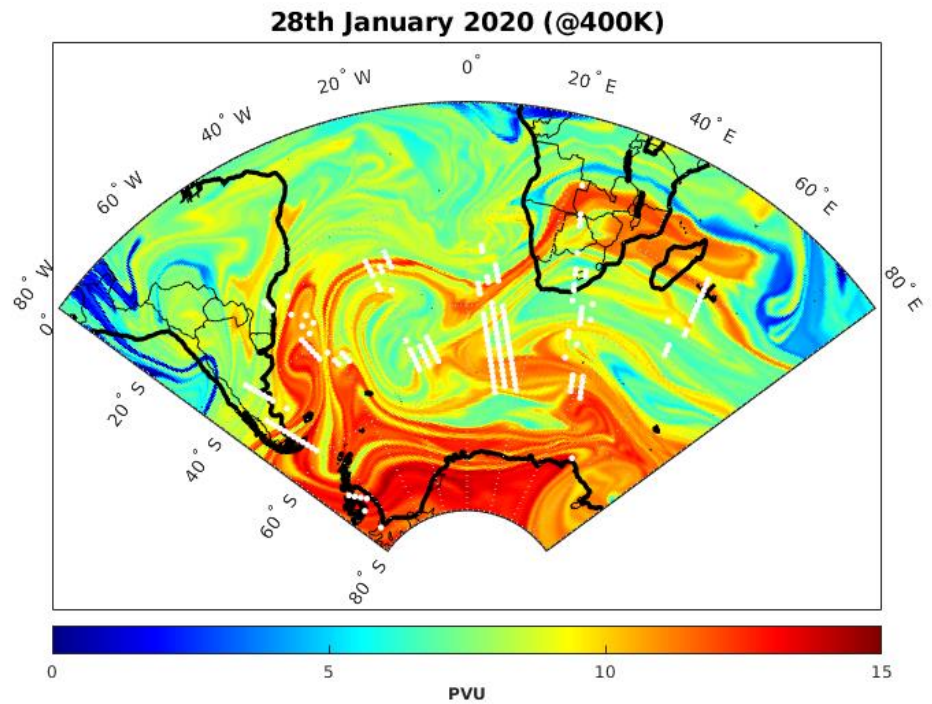

Figure 8: Advected PV map at the 400 K level obtained from the MIMOSA model (a) on 27 January 2022 and (b) on 28 January 2022. The white dots represent the localization of the aerosol plume at 400 K ± 5 K obtained from OMPS observations, while the black cross indicates Reunion.

a)

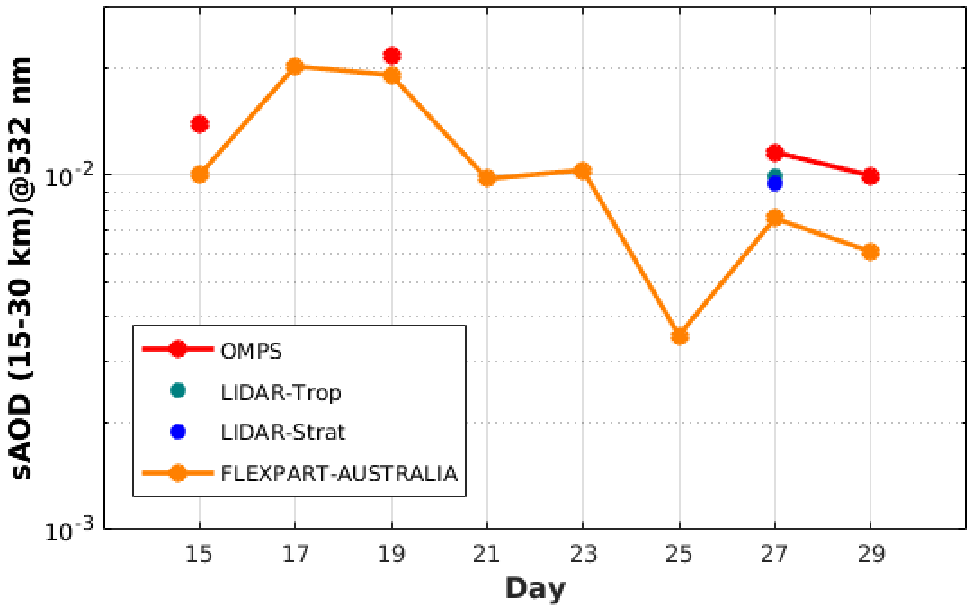

b)

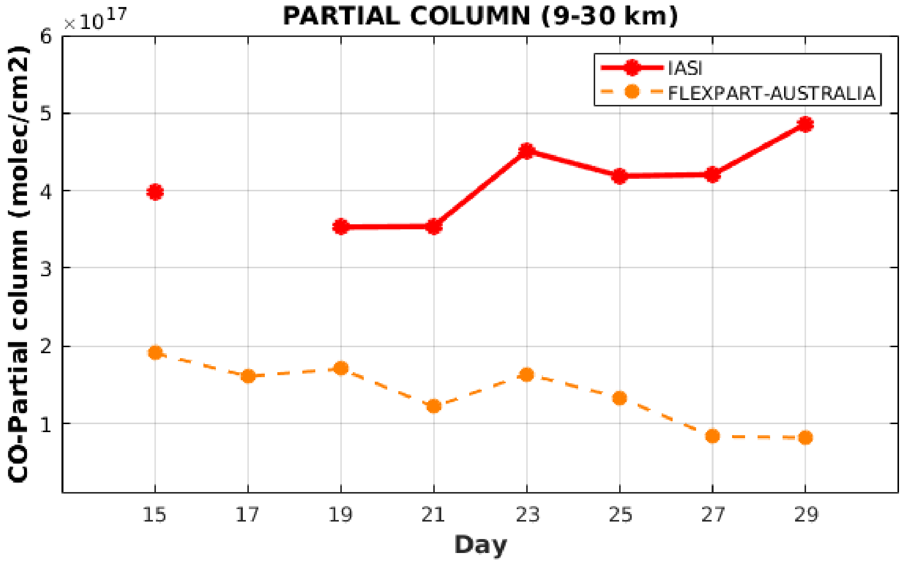

Figure 9: a) Daily evolution of sAOD (calculated between 15 and 30 km at 532 nm) obtained from OMPS-LP (red line), lidar (blue dots) and simulated by FLEXPART (orange line) over Reunion from 15th to 29th January 2020. b) Daily evolution of partial column (calculated between 9 and 30 km) of CO observed by IASI (red line) and simulated by FLEXPART (orange line) over Reunion from 15th to 29th January 2020. The CO evolution is simulated by FLEXPART considering only the CO emission (including BB and anthropogenic activity) from Australian emission. The simulated sAOD are calculated in considering only the aerosol emission (BC and OC) from Australian emission.

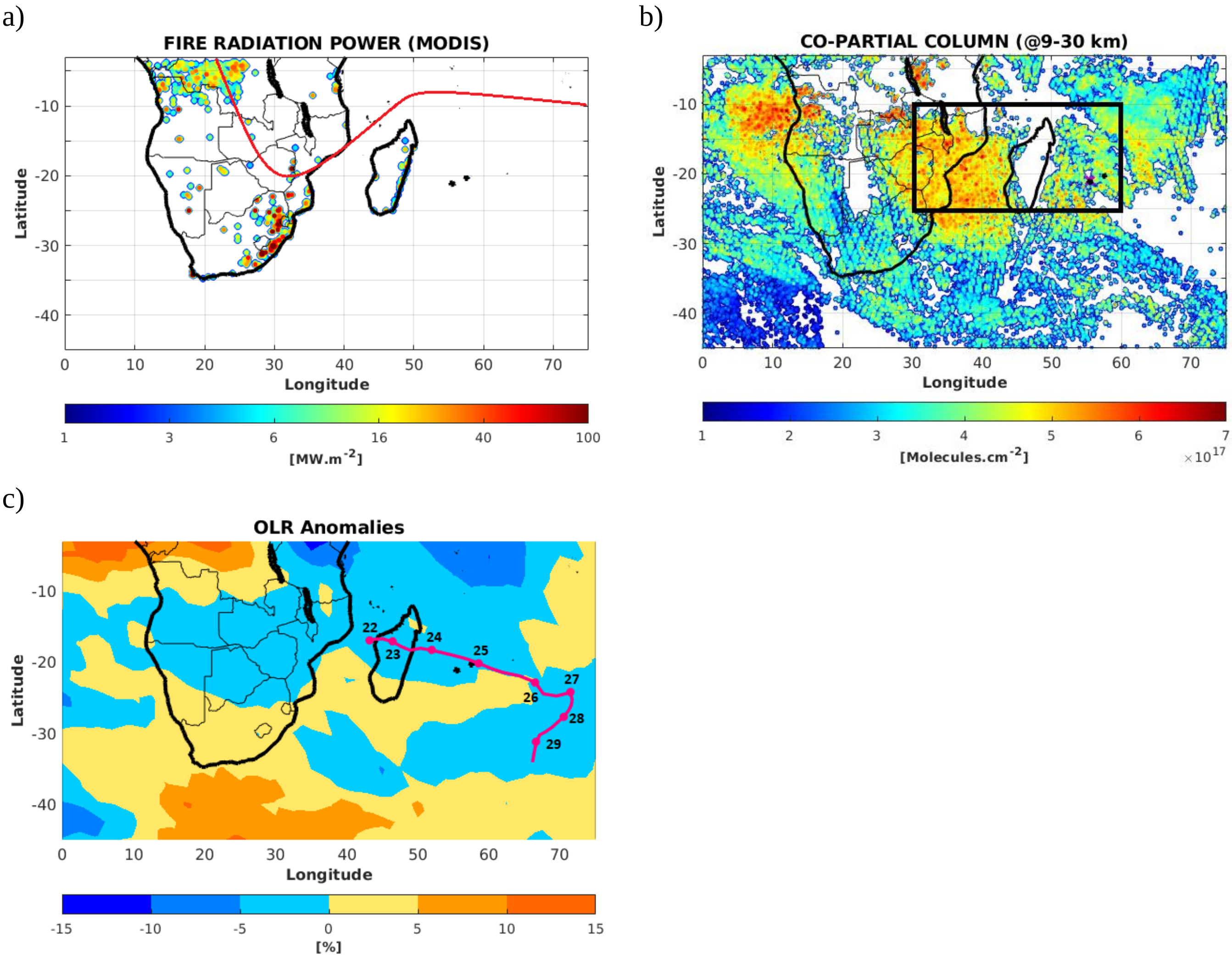

Figure 10: a) The total number of fire pixel and the associated fire radiative power obtained from MODIS observation between 16th and 29th January 2020. The red line indicates the avregae position of ITCZ (from Lashkari et al., 2017). b) Time-average map of partial column of CO (calculated between 9 and 30 km) obtained from IASI observations averaged between 16th and 29th January 2020. The black square corresponds to the study domain where the vertical cross-section of CO and water vapor mixing ratio are calculated and reported in Figure 11. c) Time-average map of outgoing longwave radiation anomalies obtained from NCEP between 16th and 29th January 2020. The red curve corresponds the trajectory followed by the Diane strong tropical storm from 22nd to 29th January 2020. This trajectory is obtained from the RSMC (Regional Specialized Meteorological Center) of Reunion best-track database.

a)

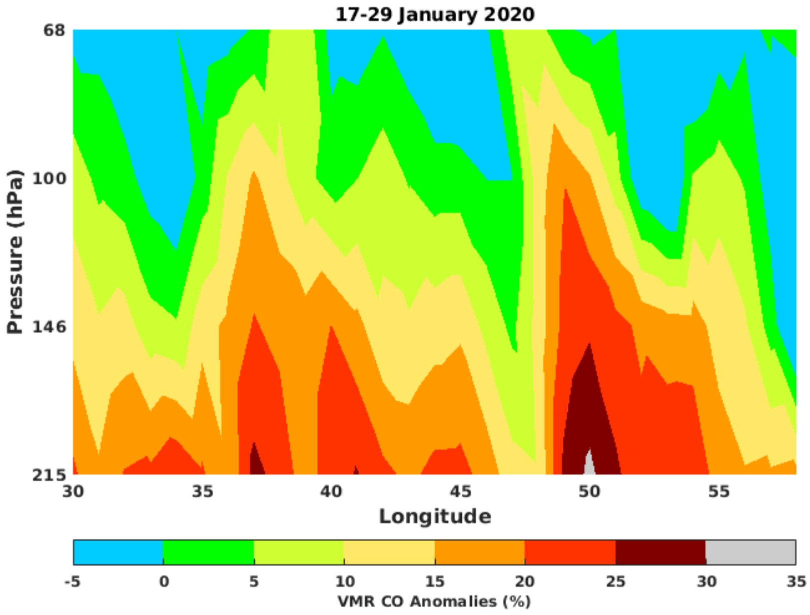

b)

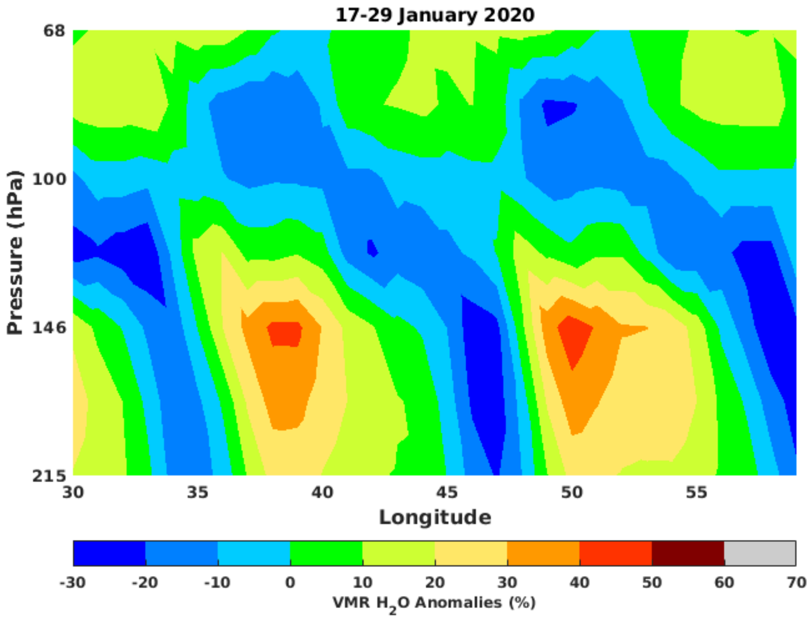

Figure 11: Vertical cross section of (a) CO and (b) water vapor mixing ratio anomalies obtained from MLS observation over southern Africa and the SWIO basin (black box in Figure 10b) between 16th and 29th January 2020.

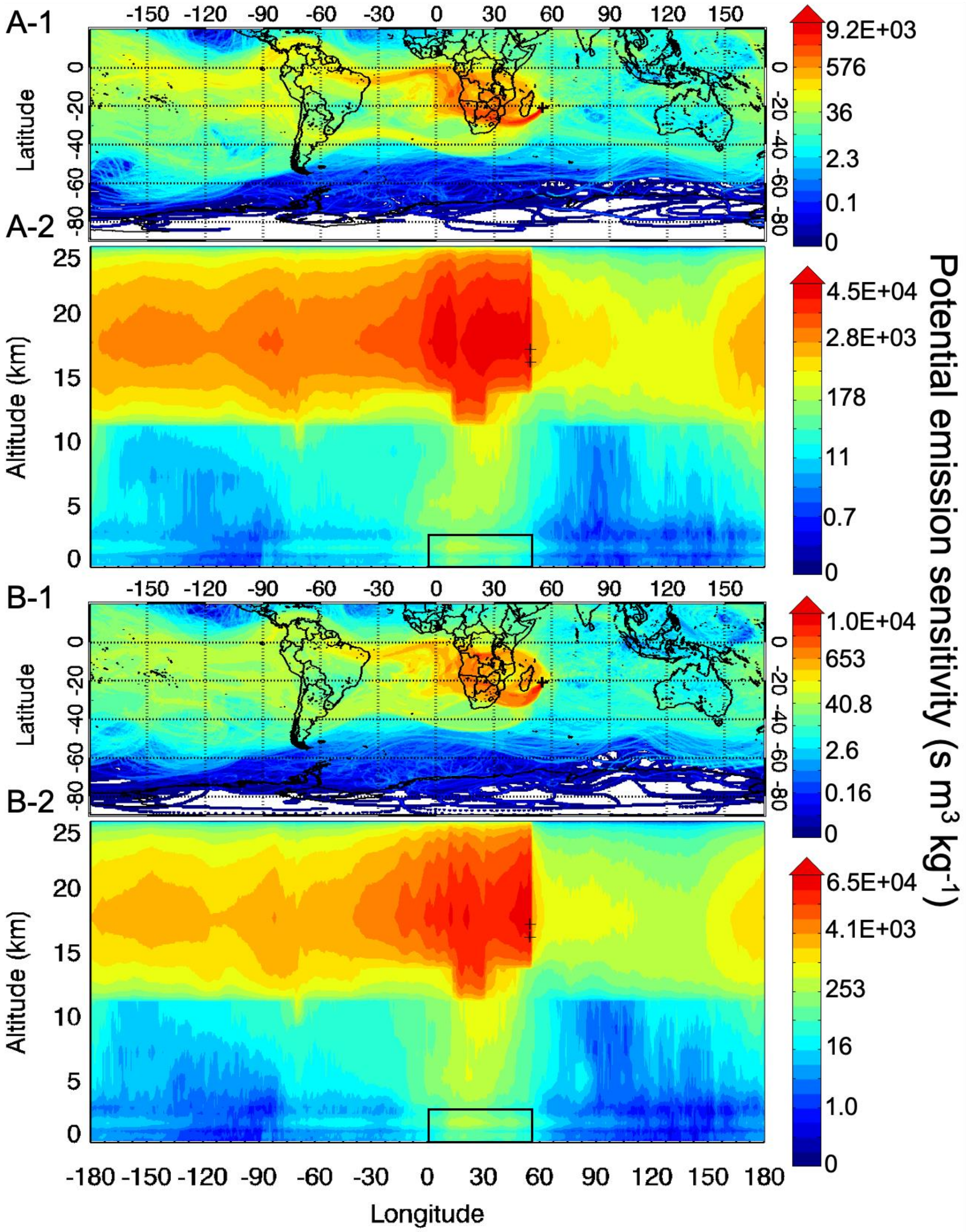

Figure 12: Same as figure 7 with an injection height initialized at 16 km.

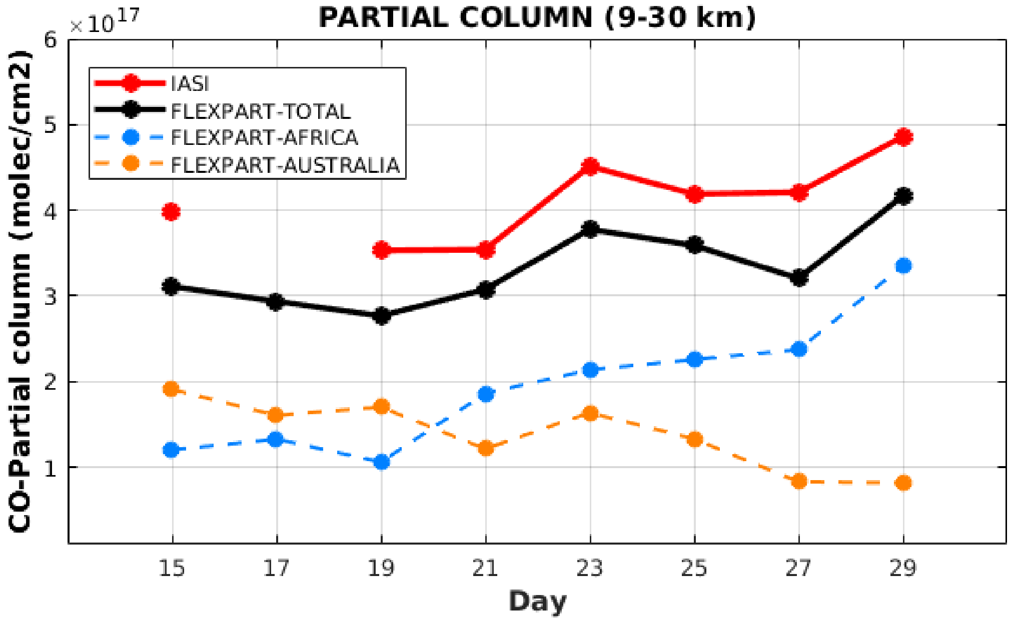

Figure 13: Daily evolution of partial column (calculated between 9 and 30 km) of CO observed by IASI (red line) and simulated by FLEXPART (black line) over Reunion from 15th to 29th January 2020. The CO evolution is simulated by FLEXPART considering only the CO emission (including BB and anthropogenic activity). The contribution from the African and Australian emission are in cyan line and orange line, respectively